External irradiation with heavy ions of neodymium silicate apatite ceramics and glass-ceramics

N. Chouard, D. Caurant, O. Majerus, J.-L. Dussossoy, P. Loiseau, C. Grygiel, S. Peuget

External irradiation with heavy ions of neodymium silicate apatite ceramics and glass-ceramics

N. Chouard[a,b], D. Caurant[a,] *, O. Majérus[a], J-L. Dussossoy[b], P. Loiseau[a], C. Grygiel[c], S. Peuget[b]

[a]Chimie ParisTech, PSL Research University, CNRS, Institut de Recherche de Chimie Paris (IRCP), UMR 8247, 11 rue P. et M. Curie, 75005 Paris, France

[b]Laboratoire d'Etude des Matériaux et Procédés Actifs, DE2D/SEVT/LMPA, 30200 Bagnols-sur-Cèze, France

[c]CIMAP, CEA/CNRS/ENSICAEN/UCBN, 14070 Caen, France

*: Corresponding author. E-mail address: daniel.caurant@chimieparistech.psl.eu (D. Caurant)

Abstract

This work aims at comparing the damage induced in the Nd silicate apatite ceramic ($Ca_2Nd_8(SiO_4)_6O_2$) by medium energy (ME) and swift heavy ion (SHI) irradiations to evaluate the effects of nuclear collisions and intense electronic excitations for ME ions and SHI ions respectively. The macroscopic induced changes were studied as a function of the fluence by swelling and hardness measurements, whereas structural modifications were followed by X-ray diffraction, Raman spectroscopy and grazing incidence EXAFS (Nd L_3-edge). At ME (1.9-6.75 MeV Au ions), radiation-induced amorphization occurred above 6.22×10^{13} Au/cm^2 associated with a volume expansion of about 8% and a drop of 37% in hardness. At SHI (90 MeV Xe ions or 35 MeV Ar ions), similar macroscopic and structural changes were observed. The electronic stopping power threshold of Nd silicate apatite for amorphization was assessed at about S_e = 5 keV/nm.

As apatite crystals containing actinides could be present in rare-earths rich nuclear glasses, SHI irradiation with Xe (995 MeV) ions was also used to damage the Nd silicate apatite crystals dispersed in a soda-lime aluminoborosilicate simplified nuclear glass over a depth of about 60 μm, to evaluate the possible formation of cracks in the residual glass due to crystals swelling. In spite of apatite crystals amorphization under SHI irradiation in the glass-ceramics, no cracking was observed in the glassy phase even close to the biggest crystals which could be explained by strain relaxation in the glass due to plastic deformation (creep) induced by SHI ion beam.

Keywords: Neodymium silicate apatite, Amorphization, Heavy ions irradiation, Glass-ceramic.

1. Introduction

Although borosilicate glasses currently remain the main kind of waste forms used to immobilize highly radioactive nuclear waste [1,2,3,4,5,6], several countries (France, Japan, United States…) have considered other alternatives to glassy matrices [7,8,9,10] mainly for specific fluxes of radioactive wastes. One of the major alternatives is to use single- or poly-phase ceramics in which radionuclides - selectively separated or not from waste solutions - could be incorporated by substitution in the crystalline structure [11,12,13,14,15,16,17,18]. Glass-ceramics consisting of crystals dispersed in a residual glass have also been envisaged and studied as potential waste forms [8,11,19,20,21]. In operating conditions and during long-term storage, these potential ceramic and glass-ceramic matrices would be submitted to severe internal radiations which could induce important atomic displacements and rearrangements frequently leading to partial or total amorphization of crystals [14]. These structural modifications could then lead to the deterioration of the integrity and long-term physicochemical properties of these matrices such as their chemical durability (radionuclides release). Therefore, one of the motivations for the studies that have been performed on such potential waste forms was to assess their susceptibility to radiation-induced defects such as the ones caused by α-decay events (recoil nuclei + α particles) due to the presence of actinides (e.g. U, Np, Pu, Am, Cm) in their structure.

During an α-decay, the α-recoil ions lose their energy in elastic collisions with the nuclei of their neighborhood and the α-particles produced deposit their energy mainly by ionization processes but also by elastic collisions at the end of its path. For β-particles and γ-radiation, the energy transfer is dominated by ionization processes [14]. The transfer of energy to nuclei by ballistic processes during α-decays causes numerous

atomic displacements: each α-particle induces several hundred displacements (near the end and along their path (16-22μm)) whereas one α-recoil ion produces highly localized cascade of 1000 to 2000 displacements over a very short range (30-40 nm) [14]. The accumulation of atomic displacements may lead to amorphization [22] (destruction of the long-range order inside the crystalline structure) and swelling (increase of the volume) [14].

Examples of ceramic matrices containing high actinide concentrations exist in nature and can serve as a source of inspiration to find efficient waste forms. For instance, in the natural fossil fission reactors located in Oklo (Gabon), rare earth (RE) and alkaline earth (M) phosphosilicate apatites (britholite) $M_{4-x}RE_{6+x}(SiO_4)_{6-y}(PO_4)_yX$ ($X = O^{2-}$, $2F^-$ or $2OH^-$) were formed that have incorporated nuclear reaction products such as lanthanides and actinides nearly 2 billion years ago [23,24,25]. Other natural phospho-silicate fluoroapatite containing actinides (U,Th) with high phosphate content were found for instance for instance in Ouzal mole (Algeria) [26] and in Russia [27]. In spite of the high doses of α-decays they received, these different natural apatite phases generally present a highly crystalline state (for instance the (U,Th)-bearing apatites from Ouzal mole have received doses up to $2.4x10^{19}$ α-decay/g i.e. about three times larger than the amorphization dose) [26,28] and still exhibit a very good chemical durability which suggests that this kind of phases could be envisaged as efficient waste forms for actinides [29,30]. The apparent lack of amorphization of these natural apatites was explained by the thermal recovery of the crystalline structure through geologic time by self-restoration of radiation damage (thermal annealing + α-annealing) [24,26,27]. Nevertheless, when increasing the number of silicate groups substituted for phosphate groups in the structure of apatite (i.e. when y decreases in the apatite formula given

above) and when increasing amount of RE^{3+} substitutes for Ca^{2+} for charge compensation reasons, its radiation resistance against amorphization is known to decrease. For instance, laboratory experiments have shown that the presence of increasing proportion of PO_4 groups at the expense of SiO_4 groups in apatite (i.e. high y values in apatite formula) was beneficial for the annealing of radiation damage by α-particles [26].

All the work performed on actinide-rich natural phases can explain why apatite ceramics have been synthesized in laboratories and studied as potential waste forms for high-level nuclear waste, particularly for actinide-rich waste streams [30,31,32,33]. For instance, the effects (amorphization, swelling) of both internal radiation by ^{244}Cm-doping [14,34,35,36,37,38,39,40] and external irradiation with heavy ions [14,33,41,42,43,44] (with energies around a few MeV) or α-particles [42,45] have been studied for purely silicate apatites such as $Ca_2RE_8(SiO_4)_6O_2$. Their crystalline structure exhibits hexagonal symmetry (space group $P6_3/m$) and consists of isolated SiO_4 tetrahedra also referred to as Q^0 units (there is no bridging oxygen atom (BO) connecting two tetrahedra) with the Ca^{2+} and RE^{3+} cations located in two sites in which actinides may also enter [46,47,48] : a 7-fold coordinated site (6h site) that is preferentially occupied by RE^{3+} cations surrounded by six oxygen atoms linked to SiO_4 tetrahedra and one isolated oxygen anion and a 9-fold coordinated site (4f site) surrounded by nine oxygen atoms linked to SiO_4 tetrahedra. The isolated oxygen anions occupy channels running through the structure along the hexagonal axis. It is important to indicate that such RE-rich silicate phases could crystallize during melt cooling in nuclear waste glasses containing RE-rich wastes [8,49,50,51,52,53,54,55] which may be problematic for the waste forms long-term containment properties. Indeed, the α self-

irradiation of these apatite crystals - that can host actinides – would induce a phase swelling and subsequent stresses and then potentially cracks in the residual glass in their surrounding and could finally lead to fragmentation of the waste forms [56] (Fig. 1) and thus to significant increase of their specific surface area. Indeed, it is known that under self-irradiation apatite crystals may become amorphous and swell, thus inducing stresses σ in the residual glass that will be proportional both to crystals swelling ΔV/V and to the cube of their size R [57]:

$$\sigma_r = -2\sigma_t = -\frac{1}{3}\frac{\frac{\Delta V}{V}}{\left(\frac{1+\nu_{RG}}{2E_{RG}}+\frac{1-2\nu_C}{E_C}\right)}\left(\frac{R}{r}\right)^3 \qquad (1)$$

where σ_r and σ_t are respectively the radial and tangential stresses induced in the residual glass by the swelling ΔV/V of a spherical particle of radius R at a distance r (r > R) from its center. ν_{RG}, E_{RG} and ν_C, E_C are the Poisson's ratio and Young's modulus of residual glass (RG) and particle (C) respectively. The stresses induced in the glass surrounding the crystals that swell are thus expected to strongly increase with their size. When envisaging immobilizing RE-rich nuclear wastes in a glass, it is thus very important to study what would be the impact of the formation of silicate apatite crystals on its long-term behavior and particularly the effect of self-irradiation on the waste form integrity.

This paper reports the study of the macroscopic and structural effects of external irradiations with heavy ions on the Nd silicate apatite $Ca_2Nd_8(SiO_4)_6O_2$ ceramic and on glass-ceramics containing crystals of this same phase dispersed in a soda-lime aluminoborosilicate glass (Nd is one of the main RE in nuclear wastes). Irradiation with

medium energy (ME) heavy ions is known to relatively well simulate the effects of α-decays (nuclear collisions) but does not enable to irradiate deeper than 2-3 μm below the surface of the glass-ceramics (Fig. 2). This is not sufficient to induce enough damage inside the apatite crystals (which size is typically several 10 μm) dispersed in the residual glass but is enough to simulate separately the effects of α-decays in totally crystalline (apatite ceramic) or in totally glassy samples. On the other hand, swift heavy ions (SHI) may deposit energy, mainly through electronic excitations, on several 10 μm depth, allowing the complete irradiation of apatite crystals and of their surrounding glass in the glass-ceramics. It was therefore necessary to firstly determine whether it was possible to simulate the effects of α self-irradiation in the apatite crystals of the ceramic with the help of the highly intensive electron excitations induced by SHI irradiations that would then enable to induce deeper damage in the glass-ceramics (~ 60 μm, Fig. 2). For this purpose, a comparative study of the damage created in the $Ca_2Nd_8(SiO_4)_6O_2$ apatite ceramic by ME and SHI ion irradiations - of respectively a few MeV and tens to hundreds of MeV - was performed in order to investigate and compare the effects of nuclear collisions and highly intensive electronic excitations. To the best of our knowledge, no studies have been reported on the comparison of the damage induced by ME and SHI ion external irradiations on such ceramics. The macroscopic changes induced in the apatite ceramic by the two kinds of irradiation chosen for this work (Xe 90 MeV or Ar 35 MeV (SHI) and Au 1.9-6.75 MeV (ME)) were studied as a function of the ion fluence by swelling and hardness measurements, and the structural modifications were followed by X-ray diffraction (XRD), Raman and X-ray absorption (Nd L3-edge EXAFS) spectroscopies.

In a second time, our objective was to study the effects of SHI irradiations (Xe 995 MeV) to a depth of about 60 µm on the structure and the microstructure of two glass-ceramic samples containing apatite crystals of different particles sizes (5-10 and 30-40 µm) dispersed in a residual soda-lime aluminoborosilicate glassy phase. The composition of the (6-oxides) parent glass used to prepare the glass-ceramics derived from that of a more complex nuclear glass envisaged to immobilize highly concentred waste (here Nd simulates all the actinides and RE present in wastes) [54,55]. This study on glass-ceramics was performed in order to try to simulate by external irradiation the effects of the internal α-decay of actinides in apatite crystals of different sizes dispersed in a simplified nuclear glass. For comparison, results concerning the macroscopic and structural changes induced by ME ion and SHI irradiations of a glass of composition similar to that of the residual glass of the glass-ceramics are also presented.

2. Experimental

2.1. Ceramics and glass-ceramics synthesis

Polycrystalline $Ca_2Nd_8(SiO_4)_6O_2$ pellets were prepared by a standard solid state process. Stoichiometric amounts of Nd_2O_3, $CaCO_3$ and SiO_2 were intimately mixed and pressed to form pellets. The pellets were then heated a first time during 24 h at 900°C (heating and cooling at 5°C/min), crushed into powders, mixed to insure homogeneity and pressed again before sintering during 100 h at 1500°C (heating and cooling at 5°C/min). According to XRD measurements, a pure apatite phase was obtained and the pellets density was measured by the Archimedes'method (d = 5.1276 ± 0.0050). Using the theoretical density (5.4667 [47]), a residual porosity of 6.21% was estimated which is pretty low for the preparation method used in this work (solid state reaction between powders). The pellets were then cut for irradiation experiments with a diamond saw in

order to obtain a square surface of about 1 cm^2 (2 mm thickness) and the specimens were polished on one side to a 1 µm diamond finish.

The nominal composition of the parent glass (PG) used to prepare the glass-ceramics and that of the residual glass (RG) synthesized using the electron probe microanalysis of the glass between the apatite crystals in the glass-ceramics are given in Table 1. The two glasses (50g per batch) were prepared using appropriate quantities of reagent grade SiO_2, H_3BO_3, Al_2O_3, Na_2CO_3, $CaCO_3$ and Nd_2O_3 powders and melted in air at 1300°C for 3h in Pt-Au (5 wt% Au) crucibles, and then cast. The glasses obtained were then ground and melted again at 1300°C for 2h to ensure homogeneity before casting on a steel plate at room temperature. Quenched glasses were amorphous according to XRD. Their density was measured by the Archimedes' method (d_{PG} = 2.8351, d_{RG} = 2.7266), the density decrease between PG and RG glasses can be explained by the Nd_2O_3 depletion in RG glass due to apatite crystallization. Their glass transformation temperature T_g (584°C (PG glass) and 572°C (RG glass)) was determined by differential thermal analysis (DTA).

Two glass-ceramics (GCA and GCB) were prepared from PG glass following a two-step thermal treatment with a nucleation step at T_g + 20°C and a growth step at 1050°C during 30h. GCA was prepared from a massive sample of PG glass whereas GCB was prepared from a powder (80-125 µm) of PG glass. This difference of glass particle sizes between the two samples before heating enabled to obtain glass-ceramics with very different microstructures as shown in Fig. 3. GCA contains only few crystals, they are rather big and elongated with the characteristic shape of apatite (hexagonal section) [51,58] and size between 10 and 100 µm depending on their orientation on the SEM image with a majority of crystals around 30-40 µm. On the contrary, GCB contains

numerous smaller crystals (5-10 μm length) dispersed in the bulk. For the two glass-ceramics, only apatite crystals were put in evidence by XRD. According to a previous work on this kind of composition, it was shown that PG glass has a strong tendency to nucleate from the surface (heterogeneous nucleation) rather than in the bulk [59]. This explains why when the specific area of the glass sample increases (as it is the case for the powder) numerous nucleation sites exist and apatite crystals grow from the surface of glass particles leading to numerous small apatite crystals (GCB). After thermal treatment, the different glass beads have sintered and the apatite crystals remain in the bulk. This kind of glass-ceramics prepared by sintering of glass powders are known as sintered glass-ceramics [60]. For the bulk glass sample much less crystals are formed in the bulk of the glass-ceramic (GCA) and due to their low quantity they easily grow and become bigger than in GCB (Fig. 3). As for the apatite ceramic pellets, samples with a surface of about 1cm^2 and 2mm thickness of GCA and GCB glass-ceramics and RG glass were cut and polished on one side for irradiation experiments.

2.2. Irradiation conditions

Two kinds of external irradiations with heavy ions were performed in this study so as to simulate the damage state induced by α-decay self-irradiation:

- ME irradiation with Au ions to damage by nuclear collisions, with similar S_n values than that of the Recoil Nucleus (RN) of an α-decay (Table 2). Because it is known that the damage state induced by α-decays is mainly controlled by the recoil nuclei, this ME irradiation condition should simulate α-decays effects in the crystalline (apatite ceramic) and residual glassy (RG glass) phases alone, these two phases being intimately mixed in the glass-ceramics (Fig. 3),

- SHI irradiations with Xe ions (90 MeV or 995 MeV) or Ar ions (35 MeV) of both the ceramics and glasses to damage by high electronic energy loss and induce ion tracks in the two previous phases alone and to compare the physical and structural effects with those of ME irradiations. Indeed, it has been shown for borosilicate glasses that SHI irradiations in the ion track regime (high S_e values) induced a similar damage state than the one induced by heavy ion irradiations in the nuclear regime (high S_n values) [61]. Therefore, these irradiation conditions should also mimic the damage induced by the RN of the α-decays. Moreover SHI irradiations (Xe ions at 995 MeV) were performed to damage by deep amorphous tracks the apatite crystals dispersed in the residual glass of the glass-ceramics GCA and GCB (Fig. 2b). The aim is to try to mimic the effects of α-decays inside the crystals and its impact on the residual glass in their surrounding that is why an irradiation depth greater than 40μm is needed for the glass-ceramic GCA with the biggest crystal size, Fig. 3a.

- *ME irradiations with Au ions*

ME heavy ion irradiations were performed on the apatite ceramic and the RG glass at room temperature with multi-energy Au ions (Au^{2+} 1.9 MeV, Au^{3+} 6.75 MeV) at the ARAMIS accelerator of the CSNSM (Orsay, France) at fluences ranging from 3.11×10^{13} up to 9.47×10^{14} ions.cm^2 (6 fluences were used). The irradiation fluences were selected to simulate deposited nuclear energies representative of those resulting from α-decay doses between 8×10^{17} and 4×10^{19} α/g (corresponding to a number of displacements per atom (dpa) between 0.07 and 3.7) to be sure to get amorphization in the ceramic at high fluence values. Indeed, according to Weber et al. [39] the ^{244}Cm doped $Ca_2Nd_8(SiO_4)_6O_2$ ceramic becomes amorphous from a dose of 2.6×10^{18} α/g (0.24

dpa). The nuclear and electronic energy losses versus ion energy were calculated with the SRIM code using the density and composition of the samples (see Fig. 4a for the apatite ceramic for 6.75 MeV Au ions, a similar tendency was obtained for the RG glass). The default SRIM values for displacement energies were used for the simulations because these values are not known for the glass. The nuclear energy loss is significant all along the ion path (Fig. 4a) contrary to the Xe high energy irradiations for which the electronic energy loss largely dominates (Fig. 4b,c). The Au ion energies were defined to obtain an almost constant ballistic damage over an irradiation depth of about 1-1.5 μm for both ceramic and glass (see Fig. 4d for the apatite ceramic, a similar tendency was obtained for the RG glass) allowing characterization of the irradiated areas with the techniques used in this study that are sensitive to a micrometric layer (XRD, microRaman, grazing incidence GI-EXAFS). Because of the low penetration depth of ME Au ions, such irradiations were not suitable to simulate the effects of α-decays in the glass-ceramics (Figs. 2a and 3). Indeed, in this case an insufficient amount of apatite crystals are irradiated to be representative of what could occur when actinides are incorporated inside. This is the reason why irradiations with heavy ions of higher energy (several hundred MeV) were performed to damage the glass-ceramics over a higher depth and affect a higher number of crystals located in a bigger volume of material (Fig. 2b).

- *SHI irradiation with Xe or Ar ions*

SHI irradiations were performed on the apatite ceramic and the RG glass at room temperature with 90 MeV Xe ions at the IRRSUD beamline of the GANIL (Caen, France) at fluences ranging from 2×10^{11} to 10^{14} ions/cm^2 (3 fluences were used). In this

case, simulations with the SRIM code showed that the initial ion energy is mainly dissipated by electronic excitation (see Fig. 4b for the apatite ceramic, a similar tendency was obtained for the RG glass) with the creation of amorphous tracks in the ceramic. Additionally, apatite ceramic and RG glass samples were also irradiated with 35 MeV Ar ions (fluence 2×10^{13} ions/cm^2) for Nd-L_3 edge EXAFS characterizations.

Table 2 summarizes the values of the projected ion ranges (R_p), nuclear (S_n) and electronic (S_e) stopping powers computed with the SRIM code for the apatite ceramic and RG glass for the two kinds of irradiation (ME : 1.9-6.75 MeV Au ions and SHI: 90 MeV Xe ions or 35 MeV Ar ions). For the ceramic, it appears that S_n is negligible as compared to S_e for 90 MeV Xe ions or 35 MeV Ar ions, whereas S_n and S_e are of the same order of magnitude for 1.9-6.75 MeV Au ions. Nevertheless, in this latter case, it is very likely that S_n leads to the macroscopic and structural modifications observed, since S_e is relatively low (<3.0 keV/nm) as compared to the value obtained for 90 MeV Xe ions (<17.5 keV/nm) and is below the threshold for damage creation (estimated at 5 keV/nm in this work, see Section 3.1.7). Finally, it is worth noting that the irradiated depth in the ceramic is much larger for 90 MeV Xe irradiations (about 9 µm) as compared to the irradiated depth for 1.9-6.75 MeV Au irradiations (1.1 µm). Nevertheless, with 90 MeV Xe ions, the irradiation depth remains too low to enable to significantly damage the glass-ceramics and more particularly for the one with the biggest crystals (GCA glass-ceramic, Fig. 3a). Profiles of deposited energy similar to those of the apatite ceramic (Fig. 4b) were obtained for the RG glass (not shown here) but the irradiated depth is slightly smaller for the ceramic because of its higher density. Similar observations than that reported above for the ceramic can be made from the S_n,

S_e and R_p values reported in Table 2 for RG glass when comparing irradiations with 1.9-6.75 MeV Au ions and 90 MeV Xe ions or Ar 35 MeV ions.

SHI irradiations at higher energy were performed with 995 MeV Xe ions at the SME line of the GANIL (Caen, France) at a fluence of 2×10^{13} ions/cm^2 at room temperature on the two glass-ceramics (GCA and GCB) to get deeper irradiation depth (> 40 μm) than with the 90 MeV Xe ions. For comparison, similar SHI irradiations with 995 MeV Xe ions were also performed on the apatite ceramic and the RG glass. Nevertheless, after irradiation with 995 MeV Xe ions and contrary to what occurred for the glass and glass-ceramics samples, the ceramic samples were totally broken and were thus not further studied (only ceramic samples irradiated with 90 MeV Xe ions were studied). As for the 90 MeV Xe ion irradiations, simulations with the SRIM code showed that the initial ion bombardment energy was mainly dissipated by electronic excitation (see Fig. 4c for the apatite ceramic, a similar tendency was obtained for the RG glass, Table 2). Contrary to irradiation with 90 MeV Xe ions of the ceramic and RG glass (see Fig. 4b for the apatite ceramic), the electronic energy loss of 995 MeV Xe ions is almost homogeneous on the whole of the irradiated depth (see Fig. 4c for the apatite ceramic). However, as it is the case for the 90 MeV Xe ion irradiations (Fig. 4b), the nuclear energy loss is only significant at the end of the ion path (Fig. 4c). These irradiations enabled to create damage at a depth of about 60 μm in the glass and 50 μm in the ceramic (Table 2) which is interesting to get a representative volume of irradiated glass-ceramics (Figs. 2b and 3).

Concerning SHI irradiations, it is important to evaluate the percentage of the surface of the samples that is affected by the amorphous tracks produced by electronic excitations. The diameter of amorphous tracks is known to depend on the electronic stopping power

of incident ions [62,63] and the lowest values reported in literature are about 5 nm [64]. With this last value and considering a random deposit of amorphous tracks, it can be shown that a fluence of about 2.10^{13} ions/cm^2 is needed to cover all the sample surface, using the following formula that gives the percentage of surface S (%) covered by tracks as a function of the fluence F (in ions/cm^2) and the track surface S (in cm^2):

$$S(\%) = 100.[1-\exp(-F.S)] \qquad (2)$$

This is the reason why in this work, we mainly performed experiments using this fluence value. Nevertheless, several SHI irradiations were also performed with lower fluences such as 2.10^{11} ions/cm^2 for which only about 4% of the samples surface was covered by tracks.

2.3. Characterization methods

The macroscopic swelling (due to the decrease in density) of the irradiated materials was determined by measuring the irradiation-induced step height on the sample surface. For this, a mask in aluminum of about 200 μm thick was placed over a part of the surface of the samples prior to irradiation. The swelling of the materials results in the appearance of a step at the slit position (Fig. 5) [65]. The step height was measured using a red-light optical interferometer. Given the projected ion range (R_p in nm) calculated by the SRIM code, the macroscopic swelling ($\Delta V/V$) resulting from irradiation can then be determined:

$$\frac{\Delta V}{V}(\%) = \frac{100Z}{R_p} \qquad (3)$$

where Z is the step height (in nm). For each characterization, the swelling represents a mean value of 6 measurements at different locations on the step.

The materials hardness before and after irradiation was measured by Vickers micro-indentation on polished specimens, with indenter loads of 10 g maintained for 5 s. This load value was optimized in order to limit the contribution to the measured hardness of the non-irradiated region of the irradiated samples below the irradiated layer (this is particularly important for ME Au ions irradiations for which the thickness of the damaged layer is thin). The Vickers hardness *Hv* was determined from the length of the diagonals of the indent according to Eq. (4):

$$Hv = \frac{2St.\sin(\frac{136}{2})}{d^2} \qquad (4)$$

where *St* is the force applied (in N) and *d* is the mean length of the indentation diagonal (in mm). For each characterization, the hardness represents a mean of 10 indentation tests.

XRD measurements were performed at room temperature with an X'Pert PRO PANalytical instrument using Cu-Kα radiation (λ = 0.15406nm). X-ray patterns were recorded at a grazing incidence of 2° for the samples irradiated with ME Au ions in order to investigate only the damaged layer on the surface (thickness of about 1 µm). In this case, the XRD patterns were recorded for 2θ ranging from 20 to 35° with a step of 0.03° 2θ and a time acquisition per step of 20 s. For the samples irradiated with SHI Xe ions, data were collected in standard (θ-2θ) geometry between 20 and 80° with a step of 0.026° 2θ and a time acquisition per step of 79 s. In this case, the maximum penetration depth of X-rays was estimated to be close to 10 µm and 75 µm for the apatite ceramic and for the glass respectively. Thus, using SHI Xe at 995 MeV, the irradiated depth of apatite phase in the glass-ceramics always remains higher (47 µm, Table 2) than the depth probed by X-rays (10 µm).

Study by Raman spectroscopy of pristine and irradiated samples was conducted at room temperature with a Raman Horiba Jobin-Yvon HR800 spectrometer equipped with an argon laser as excitation source (488 nm) for the study of the samples surface and with a Jobin-Yvon UV ARAMIS micro-Raman spectrometer equipped with a He-Cd laser as excitation source (325 nm) for the study of the samples below the irradiated surface as a function of depth along their edge after cutting. Spectrometers were equipped with a CCD detector. Spectra shown in this paper were all corrected for temperature and frequency dependency of the scattered intensity using a correction factor of the form proposed by Long [66] and were normalized to the greatest absolute intensity.

EXAFS experiments were performed at the Nd L_3-edge at the HASYLAB synchrotron on the A1 beamline (Hamburg, Germany) to investigate the environment of Nd^{3+} ions in apatite ceramic and in RG glass before and after irradiation. The effect of ME irradiation with Au ions at 1.6-9.75 MeV for 3 fluences ($6.2x10^{13}$, $3.11x10^{14}$ and $9.47x10^{14}$ ions/cm^2) inducing important nuclear interactions was compared with that of SHI irradiation with Ar ions at 35 MeV ($2x10^{13}$ ions/cm^2) mainly inducing electronic interactions and on a larger depth (Table 2). Measurements have been performed in grazing incidence and fluorescence yield mode, using a goniometer in order to investigate only the irradiated top-layer. The grazing incidence was achieved in the horizontal direction with the sample lying on the goniometer plate. The detector was a 7-cell SDD looking at the sample from the top, sample and detector being in air and at room temperature. The monochromator was a Si(111) double crystal fixed-exit monochromator. The grazing incidence angle values were 0.3° for glass samples and 1.3° for ceramic samples to achieve penetration depths of 0.5 µm in both cases (the ceramic being more dense and Nd-enriched than the glass). An angle value of 4.5° was

also used to measure at a deeper depth the ceramic irradiated at HE, but the spectra at 1.3° and 4.5° were identical so that only the 1.3° spectrum is presented here. For each measurement, about 10 scans (i.e. 5 hours of total duration) were accumulated from 6050 eV to 6720 eV, with an energy step of 0.5 eV around the edge (6208 eV), and a fixed k-step of 0.04 $Å^{-1}$ after the edge. Data analysis was performed using the Athena (XAFS extraction) and Artemis (XAFS fitting) softwares. A pre-edge line and post-edge square polynomial were used to normalize the edge. Then, the background was simulated by a spline on the 1.4 - 10 $Å^{-1}$ range with a low-r cutoff of 1.2 Å, a k-weight of 3 and medium spline clamps. The Fourier transform of the k^3-weighted XAFS oscillations ($k^3\chi(k)$) was calculated using a Hanning apodisation window on the 2.8 - 9.5 $Å^{-1}$ range with dk = 2 $Å^{-1}$. The fit of the first shell was carried out in the R-space on the 1.4 - 2.6 Å range (ceramics) or 1.5 - 2.8 Å range (glasses). All data were fitted with a single-scattering Nd-O function only, except the non-irradiated ceramic that has been fitted with two single-scattering Nd-O paths because it considerably improved the fit. The single scattering Nd-O phases and amplitudes were calculated using FEFF6 in the Artemis software, on the basis of a Nd-O distance of 2.46 Å (path 1) or 2.53 Å (path 2). These two distances exist in the $Ca_2Nd_8(SiO_4)_6O_2$ structure (Table 3). The non-irradiated $Ca_2Nd_8(SiO_4)_6O_2$ ceramic, measured at a grazing incidence angle of 1.3°, served as a reference to test the adequacy of the calculated electronic phase and amplitude parameters and fix the S_0^2 and ΔE_0 values. The Nd environment in the apatite structure is complex because Nd^{3+} ions occupy two distinct sites with different coordinations and mean Nd-O distances. Table 3 gives the details of these two sites and of an average site calculated considering the site occupancy by Nd^{3+} as reported in the ICDD 00-28-2287 reference file. As stated above, it was necessary to use two Nd-O

single-scattering paths to properly model the Nd-O shell in this material. The spectrum is shown in Fig. 11 and the results from the fit are reported in Table 4. As the test was considered satisfactory, S_0^2 = 0.95 and ΔE_0 = +5 eV were fixed in all fits using path 1. Path 2 was not used except for the non-irradiated ceramic. In all fits, the Nd coordination number was fixed at 6, in order to compare the pseudo Debye-Waller (second cumulant) parameter between the different irradiated samples.

3. Results and discussion

3.1. Irradiation of the apatite ceramic

3.1.1. Swelling measurements

Fig. 6 presents the macroscopic swelling obtained for both ME and SHI irradiations as a function of the fluence. For ME irradiations (1.9 - 6.75 MeV Au ions), swelling progressively increases with fluence and then saturates at about 8 % for an irradiation fluence exceeding 1.24×10^{14} ions/cm^2 (nuclear dose equivalent to the one induced by 3×10^{18} α/g). These results are in good agreement with those obtained by Weber et al. for a ^{244}Cm-doped apatite ceramic [34] and show that ME irradiations (nuclear collisions) provide a satisfying simulation of the macroscopic modifications induced by α-decays self-irradiation. For SHI irradiations (90 MeV Xe ions), the swelling was measured for only one fluence (2×10^{13} ions/cm^2) for which the amorphous tracks created by electronic excitations should have affected the whole surface of the sample. Thus, at this irradiation fluence, we expect a saturation value of the swelling of the apatite phase. Fig. 6 indicates that for SHI irradiation, the apatite ceramic swelling was about 5 %. It is worth noting that this value cannot possibly be compared to the value obtained with ME irradiations for the same fluence as the main mechanisms of damage are very different

in both cases (nuclear collisions for ME ions versus electronic excitations for SHI). However, this value can be compared to the saturation value obtained for ME irradiations (8 %). It thus appears that the swelling of the apatite phase is of the same order of magnitude for both kinds of irradiation but seems to be a little more important for ME irradiations (8 %) than for SHI irradiations (5 %). This may be due to the calculation method of the swelling, which considers the irradiated depth. Indeed, for SHI irradiations, the irradiated depth is higher than for ME irradiations. Consequently, it is possible that the uncertainty about the calculation of swelling is also higher. Moreover, the saturation of the swelling for the SHI irradiation may have not been totally achieved. Finally, the swelling under SHI may also have been affected by the plastic deformation usually observed in glasses and could explain a low step height value for such irradiation conditions.

3.1.2. Hardness measurements

Fig. 7 presents the Vickers hardness variation for ME and SHI irradiations as a function of the fluence. For ME (1.9 - 6.75 MeV Au ions) irradiations, the hardness progressively evolves with the irradiation fluence, in the same way as the swelling (Fig. 6). Indeed, it appears that the hardness progressively decreases with the fluence increasing, and then stabilizes at a saturation value for a fluence exceeding 1.24×10^{14} ions/cm^2, which is about 37 % lower than the initial value obtained for the pristine apatite ceramic (7300 ± 800 MPa). For SHI (90 MeV Xe ions) irradiations, the same evolution is observed, with an identical hardness decrease at saturation. These results suggest that a similar final state of material can be obtained with ME and SHI irradiations, even if the interactions are clearly different in both cases (nuclear collisions and intense electronic excitations, respectively for ME and SHI irradiations).

3.1.3. XRD measurements

Fig. 8 shows XRD patterns recorded on pristine and irradiated (at several fluences) apatite ceramic pellets with ME and SHI irradiations. For ME (1.9 - 6.75 MeV Au ions) irradiations (Fig. 8a), the diffraction peaks related to the apatite structure totally disappear between F1 and F2 fluences, that is to say between 3.11×10^{13} and 6.22×10^{13} Au/cm^2. This result indicates that radiation-induced amorphization occurred in our samples for deposited nuclear energies representative of those resulting from α-decay doses between 8×10^{17} and 2×10^{18} α/g. Besides, for the lowest fluence studied in this work (F1 = 3.11×10^{13} Au/cm^2), it appears that even if the apatite phase is still crystallized in the irradiated area, there is already a partial amorphization upon irradiation as a significant decrease of the intensity of the diffraction peaks and an important increase of their full-width at half maximum (FWHM) are observed. It is also worth noting that for this fluence, the unit cell volume increased, because the diffraction peaks position in the irradiated apatite ceramic sample shifted toward lower angles as compared to the initial position of the diffraction peaks in the pristine apatite ceramic sample (compare patterns F0 and F1 in Fig. 8a).

For SHI (90 MeV Xe ions) irradiations (Fig. 8b), the comparison between the pristine and the irradiated apatite ceramic at the first fluence (f1 = 2×10^{11} Xe/cm^2) did not reveal any evolution concerning the diffraction peaks position and their FWHM. However, a difference can be observed concerning the relative intensity of the diffraction peaks (compare patterns F0 and f1 in Fig. 8b). This can be explained by the fact that the samples are not systematically positioned the same way in the diffractometer before and after irradiation. As a consequence, it is probable that the statistic of distribution and orientation of apatite grains constituting the ceramic present in the X-ray measured

volume is different before and after irradiation, which would explain why some diffraction plans preferentially diffract as compared to others. Despite this slight difference which is not related to irradiation experiments, no structural modifications were observed for this low fluence which can be explained by the fact that less than of about 4 % of the sample surface is damaged by the amorphous tracks induced under the fluence f1. However, when the irradiation fluence increased (f2, f3), amorphization of apatite clearly occurred as the diffractions peaks of the apatite phase almost totally disappeared above f2 = 2×10^{13} Xe/cm^2. As a consequence, XRD patterns reveal that it is possible to induce amorphization of the apatite phase either by ME (1.9 - 6.75 MeV Au ions) or SHI (90 MeV Xe ions) irradiations that is to say either by nuclear collisions or intense electronic excitations.

3.1.4. Raman spectroscopy measurements

Fig. 9 shows the Raman spectra of pristine and irradiated apatite ceramic with ME and SHI irradiations for a Raman shift ranging from 200 to 1100 cm^{-1}. For the pristine apatite ceramic sample, several vibration bands can be observed and identified according to literature [67,68]. The band (a) located at 300 cm^{-1} is associated with external vibration modes, that is to say translation or libration modes of SiO_4 (Q^0) entities, Nd^{3+} or Ca^{2+} cations. The bands (b) located around 380 and 408 cm^{-1} are associated with the symmetric bending vibration modes of the SiO_4 entities (internal mode ν2). The band (c) located at about 530 cm^{-1} is attributed to the asymmetric bending vibration modes of the SiO_4 entities (internal mode ν4). The bands (d,e) located at 862 and 882 cm^{-1} are due to the symmetric stretching vibration modes of the SiO_4 entities (internal mode ν1). Finally, the bands (f,g) located at 930 and 1000 cm^{-1} are

associated with the asymmetric stretching vibrations modes of the SiO_4 entities (internal mode ν3).

By comparing the Raman spectrum of the pristine apatite ceramic sample (F0) with those of the ME irradiated samples (Fig. 9a), only few modifications are observed with increasing the irradiation fluence. This can be explained by the fact that for these irradiations, the damaged depth was only about 1 μm. Thus, it was not possible to probe only the apatite irradiated depth. Indeed, pristine apatite below the irradiated region was always more or less probed by the exciting wavelength of the Raman spectrometer and this by probing either the sample surface or the sample edge below the surface. For the 325 nm laser and the NA = 0.50 NUV objective (NA: Numerical Aperture), the depth of the laser focalization volume is estimated at 1.8 μm in air. A wider focalization depth is expected in the sample due to refraction effects. The Raman spectra presented in Fig. 9a thus correspond to the contribution of both irradiated and pristine regions of the apatite ceramic. Taking this latter statement into account, a slight shoulder (h in Fig. 9a) can be observed for high irradiation fluences (above F2) on the left side of the main vibration band (d) located at 862 cm^{-1}. An example of simulation of a part of the Raman spectrum (750-1050 cm^{-1} range) of the apatite ceramic irradiated at the fluence F3 (Fig. 10a) with Gaussian components shows the contribution of a new band (h) corresponding to this shoulder. This band could be attributed to the symmetric stretching vibration modes of the SiO_4 entities in irradiated apatite which clearly shifted toward lower frequencies (about 16 cm^{-1}) in comparison with the pristine ceramic, probably due to an elongation of the Si-O bonds. Besides, it appears that the FWHM of band h also becomes higher after irradiation and tends to saturate from $6.22x10^{13}$ ions/cm^2 (Fig. 10b), which means that there is an increase of the distribution of bond distances and angles, probably due to

an increase of the distortion of the SiO_4 tetrahedra or its surrounding. All these observations put in evidence the increase of disorder in the apatite structure, in agreement with our XRD results (amorphization, Fig. 8a). A shift of the position of the band associated with the symmetric stretching vibration modes of the SiO_4 entities toward lower frequencies and an increase of the FWHM was already observed by several authors [69,70,71,72,73,74], who studied the amorphization of natural zircon $ZrSiO_4$ containing UO_2 + ThO_2 (as in silicate apatite, only isolated SiO_4 (Q^0) entities are present in zircon). According to these authors, FWHM is characteristic of the metamict state of a material, that is to say its amorphization degree.

The Raman spectra of the SHI irradiated apatite ceramic samples (Fig. 9b) show significant differences with fluence. In this case, the irradiated depth is high enough (Table 2) to be sure to probe only the irradiated area of the samples during Raman experiments. For high irradiation fluences (from 2×10^{13} Xe/cm^2), Fig. 9b clearly brings to light a shift of the position of the main band (d) toward lower frequencies (h) (of about 22 cm^{-1}) and an increase of the FWHM similar to what was observed for ME irradiations (Fig. 10b). Moreover, for SHI irradiations, a new vibration band (of unknown origin) can be observed at about 700 cm^{-1} (band (i), Fig. 9b), this band was also slightly visible after ME irradiations (Fig. 9a). These Raman results show that despite the difference of interactions involved by ME and SHI irradiations (nuclear and intense electronic interactions respectively), similar structures have been obtained for the highest fluences (i.e. the same kind of local structural modifications have been induced by both kinds of irradiation).

3.1.5. Nd L_3-edge EXAFS measurements

The Fourier transforms of the $k^3.\chi(k)$ Nd L_3-edge EXAFS signals of the pristine apatite ceramic and of the apatite ceramic submitted to ME (1.9 - 6.75 MeV Au ions, 6.2×10^{13} or 9.5×10^{14} ions/cm^2) and SHI (35 MeV Ar ions, 2×10^{13} ions/cm^2) irradiations are shown in Fig. 11a with the corresponding fits. The results concerning the environment of neodymium in the pristine and irradiated apatite ceramic samples that can be deduced from the fit of these signals are given in Table 5. It appears that the medium-range order existing in the non-irradiated ceramic (second and third neighbor shells well visible at 3 and 4 Å in Fig. 11a) has completely disappeared in the irradiated ceramics, where no structural information is observed beyond the Nd-O first shell. The Nd-O first shell in the non-irradiated ceramic was fitted with two Nd-O contributions, one well-defined at 2.44 Å and a very distributed second contribution at a mean distance of 2.59 Å (high σ^2 and cum3 values, Table 4). For the ME irradiated ceramics, a single Nd-O contribution centered at 2.50 Å with a very large σ^2 factor (0.050 Å^2) was sufficient to fit the data (Table 5), indicating that in these samples the Nd-O shell is characterized by a strong structural disorder. The SHI irradiated sample may be less disordered comparatively to the ME samples, as suggested by lower σ^2 and cum3 values (the other parameters being identical, Table 5). However, because of the great structural disorder, it is not possible to really differentiate the two irradiated states. This result showed that both ME and SHI irradiations considerably destroy the medium-range as well as the short-range order around Nd atoms. These irradiations respectively induced mainly nuclear and electronic interactions that easily produced Nd-O disordering by atomic displacements because Nd-O bonds are mainly ionic and non-directional due to the core character of the 4f valence orbitals. It is likely that during irradiation, the Nd^{3+} and Ca^{2+} cationic sites of

the apatite structure accumulate the local defects (vacancies, interstitials) leading to the loss of long-range order, as was suggested in reference [45].

3.1.6. Comparison between ME and SHI irradiations of the apatite ceramic

Table 6 summarizes all the macroscopic and structural modifications observed in apatite ceramic samples irradiated with ME and SHI irradiations. In both cases, macroscopic modifications were quite similar with a 37% drop in hardness and a significant swelling of 8 and 5 %, respectively. Concerning the structural modifications, XRD amorphization occurred for both ME and SHI irradiations and close evolutions of the Raman spectra (shift of the position and increase of the FWHM of the band initially located at 862 cm^{-1}) were observed. Nd L_3-edge EXAFS results did not allow differentiating the damages induced either by ME or SHI irradiation because of the similar structural disorder induced in Nd surrounding. As a consequence, according to our results it appears that the final state of the apatite phase is comparable for both kinds of irradiations, despite the fact that the mechanisms of damage production are very different (nuclear collisions or intense electronic excitations). Thus, it seems to be possible to simulate α decay self-irradiation induced amorphization in apatite with nuclear interactions as well as with high electronic excitations.

3.1.7. Electronic stopping power threshold (S_e) for amorphization of the apatite ceramic

Amorphization by intense electronic excitation may be achieved if the ion electronic stopping power exceeds a threshold value, which depends on the nature of the crystalline phase. For $Ca_2Nd_8(SiO_4)_6O_2$ apatite, this threshold was estimated by recording the evolution with depth of the Raman spectrum of the apatite ceramic (Fig.

12a) irradiated with Xe ions (90 MeV, 2×10^{13} ions/cm^2). By following the evolution with depth from the irradiated ceramic surface of the FWHM of the band associated with the symmetric stretching vibrations of SiO_4 Q^0 entities (located at 862 cm^{-1} in the pristine $Ca_2Nd_8(SiO_4)_6O_2$ apatite ceramic) and by comparing it with the evolution of S_e with depth as calculated by SRIM (Fig. 12b), it appears that above S_e = 5.2 keV/nm total amorphization of apatite is observed whereas below S_e = 0.8 keV/nm apatite remained totally crystalline. Thus, the threshold electronic stopping power of Nd silicate apatite is about S_e = 5 keV/nm.

3.2. Irradiation of the residual glass

3.2.1. Swelling and hardness measurements

Fig. 13 presents the macroscopic swelling and hardness variation obtained for the residual glass (RG glass) submitted to ME irradiations (1.9 - 6.75 MeV Au ions) as a function of the fluence. It appears that swelling remains close to about 1% for all fluences (Fig. 13a). This value is in accordance with that reported in literature for other irradiated glasses [75,76,77]. The lack of significant evolution of swelling with fluence indicates that its maximal value was reached from the lowest fluence (3.1×10^{13} ions/cm^2). In accordance with these swelling results, a decrease of about 33% of glass hardness was observed for all fluences (Fig. 13b). This decrease of hardness is in accordance with the values reported in literature for self-irradiated Cm-doped and externally irradiated (with multi-energy Au ions) borosilicate glasses [76,77,78].

Swelling and hardness measurements were also carried out on the RG glass after SHI irradiation with 90 and 995 MeV Xe ions. To determine the swelling for these two SHI irradiations (fluence 2×10^{13} ions/cm^2), we firstly compared the implantation depth Rp

determined by the SRIM code (11 and 61 μm respectively for 90 and 995 MeV Xe ions) with the damaged depth determined by following the evolution of Raman spectra of irradiated RG glass versus the distance from sample surface assuming that as long as the spectrum remained different to that of the pristine glass the Raman laser beam was probing the region of the glass damaged by SHI irradiations (11 and 54 μm respectively for 90 and 995 MeV Xe ions). To determine experimentally the depth of damaged RG glass, a piece of sample was cut and polished on the edge, and Raman spectra were recorded as a function of depth along the direction perpendicular to the irradiated surface. It appeared that for the irradiation with 995 MeV Xe ions the damaged depth was slightly lower than the implanted depth whereas for the irradiation with 90 MeV Xe ions the depth values were similar. To calculate swelling from equation (2) we thus used the damaged depth rather than the implanted depth Rp. It appeared that swelling decreased with Xe ions energy from 0.50% for 90 MeV Xe ions to 0.20% for 995 MeV Xe ions. These values are lower than the ones obtained after ME irradiation with 1.9 - 6.75 MeV Au ions (~ 1%, Fig. 13a). The decrease of swelling with ions energy could be explained by the possible occurrence of increasing glass creep that would also induce partial stress relaxation during SHI irradiation (see Section 3.3.5.). Nevertheless, for the same fluence (2×10^{13} ions/cm^2) no significant variation of hardness with Xe ions energy was observed whereas a significant evolution of hardness was put in evidence with the fluence between 2×10^{11} and 2×10^{13} ions/cm^2 for 90 MeV Xe ions (Fig. 13c).

3.2.2. Raman spectroscopy measurements

The structural evolution of the glassy network of RG glass after irradiation with ME and SHI was followed by Raman spectroscopy. For ME irradiations (1.9 - 6.75 MeV Au

ions), the damaged depth is about 2 μm (Fig. 4d) which is smaller than the laser focalization depth in the samples. Only a slight evolution of Raman spectra was observed with increasing the fluence from 3.11×10^{13} to 9.47×10^{14} ions/cm^2. For instance, the spectra of RG glass before and after irradiation with the highest fluence (9.47×10^{14} ions/cm^2) are shown in Fig. 14a. Concerning the low energy region of the spectra (500-600 cm^{-1}), a slight shift towards higher wavenumber (~10 cm^{-1}) was observed after irradiation for the bands associated with Si-O-Si vibrations (*a* and *b* bands in Fig. 14a). According to literature [77,79,80] this shift could be attributed to a reduction in the Si-O-Si bond angle between silica tetrahedra and could indicate an increase of the depolymerization of the silicate network (i.e. increase of the amount of non-bridging oxygen atoms (NBOs)) after irradiation as shown by molecular dynamics [81]. Nevertheless, in this study, the lack of significant evolution of the broad and high-intensity band between 850 and 1200 cm^{-1} associated with the stretching vibration of Q^n units (i.e. SiO_4 units with n bridging oxygen atoms) does not seem to confirm any significant irradiation-induced depolymerization of the silicate network. Indeed, only a very slight shift towards higher wavenumber of the Q^3 contribution (~1050 cm^{-1}, *g* in Fig. 14b) and towards lower wavenumber of the Q^2 contribution (~950 cm^{-1}, *h* in Fig. 14b) was detected after irradiation. This slight evolution of the position of the Q^3 and Q^2 contributions after irradiation indicates a slight evolution of the environment of the corresponding SiO_4 tetrahedra that could be due for instance to the increase of the proportion of Na^+ ions in the neighbouring of Q^n units. Indeed, Neuville [82] reported that the progressive substitution of CaO by Na_2O in a SiO_2-Na_2O-CaO glass induced a shift of the Q^3 (1050 cm^{-1}) and Q^2 (950 cm^{-1}) bands respectively to higher and lower wavenumber as observed in the present study (Fig. 14b). However, it appeared that

irradiation induced a significant increase of the intensity of the band attributed to the vibration of depolymerized BO_3 units between 1300 and 1600 cm^{-1}. This evolution could be correlated to the slight intensity decrease of the spectrum around 780 cm^{-1} (d in Fig. 14a), a spectral region classically attributed to the vibration of borate rings with BO_4 units [83]. Thus, in accordance with several structural results reported in literature on irradiated borosilicate glasses [77,80,84], a fraction of the BO_4 units present in the RG glass before irradiation may have transformed into BO_3 units after irradiation releasing charge compensators such as Na^+ cations (initially used for the charge compensation of the negatively charged BO_4 units) and non-bridging oxygens (NBO) in glass structure. For instance, ^{11}B MAS NMR and molecular dynamics studies have reported the partial transformation of BO_4 into BO_3 units under heavy ions irradiation or α decay self-irradiation and proposed that the structural evolution under irradiation (disorganization + reconstruction of glass structure) could be interpreted as freezing a glass structure with higher fictive temperature than pristine glass [77,80,81,85].

For SHI irradiations of RG glass with 90 MeV Xe ions at various fluences (from 2×10^{11} to 1×10^{14} ions/cm^2, Fig. 15) or with 995 MeV Xe ions at only one fluence (2×10^{13} ions/cm^2, spectrum not shown), the Raman spectra correspond to the contribution of the irradiated layer only. An evolution of Raman spectra similar to that of the RG glass submitted to ME irradiations was observed. Indeed, a shift towards higher wavenumber of the bands in the low energy region (500-600 cm^{-1}, Fig. 15a), an increase of the relative intensity of the band attributed to the vibration of BO_3 units (1300-1600 cm^{-1}, Fig. 15a) and a slight shift of the contribution of the Q^3 and Q^2 units (at about 950 and 1050 cm^{-1} respectively, Fig. 15b) were put in evidence for the two kinds of SHI irradiations with fluence greater than or equal to 2×10^{13} ions/cm^2. For lower fluence

(2×10^{11} ions/cm^2, 90 MeV Xe ions), the Raman spectrum remained similar to that of the pristine RG glass (Fig. 15) because only a small fraction (~ 4%) of the sample surface was affected by amorphous tracks as indicated above whereas for higher fluence ($\geq 2\times10^{13}$ ions/cm^2) almost all the surface was affected.

As for the apatite ceramic, the comparison of the Raman results for ME and SHI irradiations (corresponding mainly to nuclear and electronic interactions respectively) show that despite the difference of interactions involved in, similar structural modifications have been put in evidence for the two kinds of irradiation.

3.2.3. Nd L_3-edge EXAFS measurements

The Fourier transforms of the $k^3.\chi(k)$ Nd L_3-edge EXAFS signals of the pristine and irradiated RG glass with ME (1.9 - 6.75 MeV Au ions, 6.2×10^{13} or 3.1×10^{14} ions/cm^2) and SHI (35 MeV Ar ions; 2×10^{13} ions/cm^2) irradiations are shown in Fig. 11b, together with their corresponding fits. The results concerning the environment of neodymium in the pristine and irradiated glass that can be deduced from the fit of the first shell are given in Table 5. The Nd-O shell in the non-irradiated glass was properly modelled using a single scattering Nd-O path and third and fourth cumulants (R-factor = 0.0016). The Nd-O mean distance is 2.45 ± 0.03 Å and the pseudo Debye-Waller factor is σ^2 = 0.025 ± 0.006 Å^2, in agreement with previous results on similar glasses [86]. In the irradiated glass samples, the Nd-O mean distance is unaffected but the disorder has greatly increased as shown by larger values of the σ^2 and third cumulant parameters. It is interesting to notice that despite its initial disorder, the RG glass undergoes additional disordering on the short-range scale due to ME or SHI irradiation. As for the Raman characterizations presented above, it is not really possible once again to differentiate the

structural effects of the different kinds of irradiation (ME and SHI), because of the large structural disorder combined with a low r-space resolution. This low r-space resolution is due to the narrow k-range measured (that is limited by the Nd L_2-edge at 6721 eV) and to the dampening of the EXAFS oscillations induced by the disorder. However, we can note that SHI irradiation did not cause such a large disorder as the ME irradiation with the highest fluency (3.1×10^{14} ions/cm^2). In this latter case, the elevated third cumulant value and the reduced quality of the fit both indicate that the disordering of the Nd-O shell is strongly dissymmetrical and cannot be well fitted using one Nd-O contribution only.

3.2.4. Comparison between ME and SHI irradiations of the residual glass

Table 7 summarizes all the macroscopic and structural modifications observed in RG glass samples irradiated with ME and SHI irradiations. In both cases, macroscopic modifications were similar: 33-35% drop in hardness and swelling ≤ 1 %. Concerning the structural modifications of the glassy network, close evolutions of the Raman spectra were observed for the two kinds of irradiation for fluence ≥ 2×10^{13} ions/cm^2: shift towards higher wavenumber of the bands in the low energy region (500-600 cm^{-1}) indicating a decrease of the Si-O-Si angle, increase of the relative intensity of the band attributed to the vibration of BO_3 units (1300-1600 cm^{-1}) indicating partial transformation of BO_4 into BO_3 units and slight shift of the contribution of Q^2 and Q^3 units (at about 950 and 1050 cm^{-1} respectively) probably due to slight modification of the neighboring of these units. The Nd-O shell undergoes disordering with respect to the pristine state, as put in evidence by larger values of the σ^2 and third cumulant parameters in the fit of the Nd L_3-edge EXAFS, using a model of one Nd-O single

scattering contribution. The description of this structural disordering is limited by the low r-space resolution. Subject to this limitation, the Nd-O disordering is similar for ME and SHI irradiations, with the highest level of disorder measured for the highest fluency at low energy. Consequently, as for the apatite ceramics presented above, it appears that the final state of RG glass is comparable for both kinds of irradiations (ME and SHI), despite the differences of damage mechanisms. SHI irradiation can thus be used to generate a final state of the glass close to that induced by nuclear collisions from α-decays.

3.3. Irradiation of the apatite-based glass-ceramics

In order to simulate the effects of the α-decay of actinides that could be incorporated in the neodymium silicate apatite crystals dispersed in partially crystallized glass samples, we present and compare in this last part the results obtained by external SHI irradiations (Xe 995 MeV, fluence 2×10^{13} ions/cm^2) of the GCA and GCB glass-ceramics containing apatite crystals of different sizes (Fig. 3). Such irradiations induce deeper damage (~ 60µm irradiation depth) than 90 MeV Xe (about 9 µm) and 1.9-6.75 MeV Au (1.1 µm) irradiations which enables to irradiate a larger volume of glass-ceramic (Fig. 2). We focussed here our interest on the evolution after irradiation of the physical properties, microstructure and structure of the two glass-ceramics. As we saw in previous sections that the crystalline (apatite) and glassy phases exhibit separately different swelling behaviors under SHI irradiation, a particular focus was put here on the formation or not of micro-cracking in the glassy phase surrounding the crystals and particularly on the impact of the size of crystals.

3.3.1. XRD and Raman spectroscopy

As it was the case for the apatite ceramic irradiated with SHI 90 MeV Xe ions (Fig. 8b), XRD measurements showed that the apatite crystals located close to the surface of the two glass-ceramics became totally or almost totally amorphous under irradiation with SHI 995 MeV Xe ions (Fig. 16). This was confirmed by the evolution after irradiation of the Raman spectra of apatite crystals close to the surface of GCA and GCB samples (Fig. 17) which showed an evolution similar to that of the apatite ceramic presented above (Section 3.1.4). Indeed, a shift from 862 cm^{-1} to 842 cm^{-1} of the position of the main band associated with the vibration of the SiO_4 (Q^0) entities was put in evidence for the two samples associated with an increase of the FWHM of about 26 cm^{-1} (compare to Table 6). The evolution of the structure of the residual glass after irradiation was also followed by Raman spectroscopy for the two glass-ceramics by probing the glass between apatite crystals with the laser beam. An evolution very similar to that of the glass presented above (Section 3.2.2.) was observed for GCA and GCB samples (spectra not shown) indicating similar structural evolution concerning particularly SiO_4 (Q^n), BO_4 and BO_3 units.

3.3.2. Microscopic characterization

SEM images of the surface of the glass-ceramic GCA with the biggest apatite crystals before and after SHI irradiation (Xe 995 MeV, fluence 2×10^{13} ions/cm^2) did not reveal any cracking in the residual glass induced by irradiation (Fig. 19 a,b). The only cracks observed on the images were already present before irradiation and were probably formed during the thermal cycle of the fabrication step due to the difference of thermal expansion coefficient between crystals and residual glass. Similar observations were

done for the glass-ceramic GCB except that in this case no cracks were observed before irradiation probably because of the smallest crystals size (images not shown). SEM observations were also performed in the bulk (below the irradiated surface) of the two glass-ceramics after samples cutting and polishing perpendicular to the irradiated surface (Fig. 18c,d). As for surface SEM observations, no cracks induced by SHI irradiation were put in evidence for GCA and GCB samples. Thus, contrary to what was expected from results reported in literature on the generation of cracks in the glass surrounding apatite and pyrochlore crystals containing actinides, both of which became amorphous due to self-irradiation [16,87], we did not observe this effect in our glass-ceramic samples irradiated by SHI even for the sample containing the biggest apatite crystals. As proposed below, this lack of cracking is probably due to the creep of the residual glass during irradiation that would be responsible for the relaxation of the stress induced by crystals amorphization.

3.3.3. Swelling and hardness measurements

Because of the presence of two phases (residual glass + apatite crystals) in GCA and GCB glass-ceramics, it was very difficult to quantify precisely the swelling induced by SHI irradiation (995 MeV Xe ions, 2×10^{13} ions/cm^2). Nevertheless, a value of about 0.4% was estimated for the two samples. This value is slightly higher than the swelling of the RG glass irradiated in the same conditions (0.2%) but is much lower than the swelling of apatite ceramic (5%). The fact that glass-ceramics swelling is higher than that of RG glass can be explained by the presence of crystals. Concerning hardness measurements, it was possible to determine the effect of SHI irradiation on the residual glass between apatite crystals but not for the crystals because of their too small size

(penetration of the indenter in the residual glass surrounding crystals during measurement). The variation of Vickers hardness of the glassy phase in GCA and GCB glass-ceramics after SHI irradiation (~ -33%) was very close to that of the totally amorphous RG glass sample (-33 to -35%, Table 7). Thus, under SHI irradiation the residual glass surrounding apatite crystals seems to behave in the same way as the RG glass that does not contain apatite crystals. This is in accordance with Raman results that indicated similar structural evolution of the glassy phase for the RG glass and the two glass-ceramics.

3.3.4. Evolution of the surface of glass-ceramics

An optical microscopy image of the surface of the glass-ceramic with the biggest crystals (GCA sample) after SHI irradiation is shown in Fig. 19a. As the surface was partially covered with an aluminum mask protecting the underlying glass-ceramic against irradiation, it was possible to directly observe the effect of SHI irradiation by comparison with the pristine glass-ceramic on the same sample. The interface between irradiated and non-irradiated zones clearly appears on the image and it seems that apatite crystals that were present on the surface before irradiation sank into the glass after irradiation as if the glass had softened around them during irradiation. Crystals sinking close to the surface was confirmed by studying the step height (Fig. 19b) and 3D topographic (Fig. 19c) profiles obtained with the scanning interferometer which could be explained by creep of the residual glass under SHI irradiation. Indeed, it is known that under energetic ion bombardment, due to viscosity reduction resulting from the accumulation of atomic displacements and local heating, amorphous materials (oxides, metals) may exhibit plastic deformation (expansion) in the plane perpendicular

to the ion beam, i.e. hammering effect [88,89,90]. We propose that it could be the impediment by the crystals of the residual glass creep in the direction perpendicular to the ion beam that would explain the apparent crystals sinking on the glass-ceramic surface (under irradiation the glass of reduced viscosity would rise on the edge of the crystals).

3.3.5. Comment on the simulation by SHI irradiation of α-decays in the apatite-based glass-ceramics

Our aim was to simulate by external SHI irradiation the swelling of apatite crystals dispersed in a borosilicate glass that would result from amorphization under the α-decays emitted by actinides incorporated in their structure (self-irradiation) and to check the effect of crystals size on the formation of cracks in the residual glass due to the stress accumulation linked to differential swelling behavior between the crystals and the glass. The results presented above showed that independently of the size of apatite crystals, no crack formation was put in evidence in the glassy phase in spite of crystals amorphization. Our observations are thus different to the ones reported in literature on the formation of cracks in glasses due to amorphization of apatite and pyrochlore crystals containing actinides [16,87], but in our case the creep of the glassy phase under the Xe ions beam is probably responsible for the relaxation of the stresses [88,91,92] induced in the glass by crystals swelling during amorphization and thus for the lack of cracks detection even at proximity of the biggest crystals. Consequently, concerning the matrix studied in this work, we cannot conclude if cracks would form or not under α decay self-irradiation during the storage of the partially crystallized glass containing actinide-bearing apatite crystals.

Literature [89,92] indicates that creep phenomena under heavy ion beams occurs in glassy materials only if the electronic stopping power S_e of the ions is high enough and starts only after an incubation dose related to S_e. This suggests that in our experiments the electronic stopping power of the 995 MeV Xe ions (S_e = 17.5 keV/nm, Table 2) was probably too high and the fluence (2×10^{13} ions/cm^2) was probably higher than the incubation one. To complete this work, in order to succeed to simulate the effects of α decay self-irradiation in the glass-ceramics and particularly the stress induced in the residual glass by crystals swelling, it would be interesting to perform other SHI ions irradiation experiments with lower S_e keeping the fluence below the incubation limit in order to avoid stress relaxation in the glassy phase during irradiation. Nevertheless, in order to maintain the amorphization of the crystalline phase during these experiments, it will be important to keep S_e above the amorphization threshold of apatite that was estimated at 5 keV/nm.

4. Conclusion

This study was an attempt to simulate the effects of α-decay in glass-ceramics bearing the $Ca_2Nd_8(SiO_4)_6O_2$ apatite phase, by the mean of SHI to irradiate a large volume of material encompassing crystals and residual glass. A first step was to compare SHI irradiation, which deposits energy by intense electronic excitations, with medium energy (ME) heavy ion irradiation, which deposits energy essentially by nuclear collisions and is therefore considered as more representative of α decay self-irradiation. This comparison was performed in the two separate phases, the apatite ceramic and the residual glass, at macroscopic and microscopic scales. For both phases, ME and SHI irradiation produced very comparable amounts of swelling and Vickers hardness

decrease. The silicate apatite amorphized under ME irradiation for an irradiation fluence in between 6.2×10^{13} and 1.2×10^{14} ions/cm^2 (nuclear damage in between 0.25 and 0.5 DPA) in good agreement with the amorphization dose reported for a ^{244}Cm-doped apatite ceramic of same composition, confirming the relevance of ME irradiation to simulate α decay self-irradiation. The silicate apatite also amorphized under SHI irradiation, with an electronic stopping power threshold estimated at around 5 keV/nm. Raman and Nd L3-edge EXAFS examination indicated that the resulting amorphous structures were similar for both irradiations. Concerning the borosilicate glass, similar structural variations were also observed, with the interesting finding that ME or SHI irradiation significantly impact the short-range order around Nd^{3+}, by broadening the Nd-O distance distribution with respect to the pristine glassy state. Therefore, at least in the case of the two phases concerned in this study, we propose to consider that ME and SHI irradiations produce macroscopic and structural damages comparable to self-irradiation by α-decay, although the nature of the interaction between the incident ions and the material is different (nuclear collision for ME, intense electronic excitations for SHI). In a second step, glass-ceramics bearing $Ca_2Nd_8(SiO_4)_6O_2$ crystals of different sizes (either 5-10 µm, or 10-100 µm), were irradiated with SHI irradiation over a depth of about 60 µm. The appearance of cracks was expected in the glass surrounding the biggest crystals, due to the stress induced by the swelling and differential mechanical properties of the two phases. No such crack could be observed, but rather a sinking of the crystals and a rise of the glass on their edge that may be explained by the creep of the glass in the direction perpendicular to the ion beam. From this result, better SHI irradiation conditions may be proposed to induce amorphization of the apatite crystals

while avoiding stress relaxation in the glass by creep phenomena, allowing the proper study of the glass-ceramic integrity under α-decay irradiation.

Acknowledgments

The authors gratefully acknowledge the CEA and the Chaire ParisTech "Ingénierie Nucléaire'' funded by Areva for the financial support of this study. The authors also acknowledge the ARAMIS staff of the CSNSM (Orsay, France) for assistance during irradiation experiments and the members of the HASYLAB synchrotron source (A1 beamline, Hamburg, Germany) for their help and availability during EXAFS experiments. R. Baddour-Hadjean and J-P. Pereira Ramos from the GESMAT/ICMPE (Thiais, France) and D. de Ligny from the FAU (Erlangen-Nürnberg, Germany) are gratefully acknowledged for giving the possibility to the authors to use their Raman spectrometers for samples characterization.

References

[1] C.M. Jantzen, Development of glass matrices for high level radioactive waste, in Handbook of Advanced Radioactive Waste Conditioning Technologies, Ed. M. I. Ojovan, Woodhead Publishing Series in Energy, Cambridge (2011) 230-292.

[2] M.I. Ojovan, W.E. Lee, New developments in glassy nuclear wasteforms, Nova Science Publishers, New York (2007).

[3] E. Vernaz, S. Gin, C. Veyer, Waste glass, in Comprehensive Nuclear Materials Vol. 5, Ed. R. J. M. Konings, Elsevier, Amsterdam (2012) 451-483.

[4] I.A. Pegg, Turning nuclear waste into glass, Phys. Today 68(2) (2015) 33-39.

[5] M.I. Ojovan, O.G. Batyukhnova, Glasses for nuclear waste immobilization, Proc. WM'07 Conference, Tucson (2007) (www.wmsym.org/archives/2007/pdfs/7061.pdf).

[6] S. Gin, P. Jollivet, M. Tribet, S. Peuget, S. Schuller, Radionuclides containment in nuclear glasses: an overview, Radiochim. Acta 105 (2017) 927-959.

[7] I.W. Donald, Waste immobilization in glass and ceramic based hosts. Radioactive, toxic and hazardous wastes. Wiley, Chichester, (2010).

[8] D. Caurant, P. Loiseau, O. Majérus, V. Aubin-Chevaldonnet, I. Bardez, A. Quintas, Glasses, glass-ceramics and ceramics for immobilization of highly radioactive nuclear wastes, Nova Science Publishers, New York (2009).

[9] M.I. Ojovan, W.E. Lee, An Introduction to Nuclear Waste Immobilization, Elsevier, Amsterdam (2005).

[10] W.J. Weber, A. Navrotsky, S. Stefanovky, E.R. Vance, E. Vernaz, Materials science of high-level nuclear waste immobilization, MRS Bull. 34 (2009) 46-53.

[11] I.W. Donald, B.L. Metcalfe, R.N. Taylor, The immobilization of high level radioactive wastes using ceramics and glasses, J. Mater. Sci. 32 (1997) 5851-5887.

[12] B.E. Burakov, M.I. Ojovan, W.E. Lee, Crystalline materials for actinide immobilization. Materials for Engineering Vol.1. Imperial College Press (2011).

[13] A.E. Ringwood, S.E. Keeson, K.D. Reeve, D.M. Levins, E.J. Ramm, SYNROC, in Radioactive Waste Forms for the Future, Eds. W. Lutze and R. C. Ewing, Elsevier Science Publishers B. V. (1988) 233-333.

[14] E.R. Vance, Ceramic waste forms, in Comprehensive Nuclear Materials Vol. 5, Ed. R. J. M. Konings, Elsevier, Amsterdam (2012) 485-503.

[15] H. Kinoshita, Development of ceramic matrices for high level radioactive wastes, in Handbook of Advanced Radioactive Waste Conditioning Technologies, Ed. M. I. Ojovan, Woodhead Publishing Series in Energy, Cambridge (2011) 293-338.

[16] W.J. Weber, R.C. Ewing, C.R.A. Catlow, T. Diaz de la Rubia, L.W. Hobbs, C. Kinoshita, Hj. Matzke, A.T. Motta, M. Nastasi, E.K.H. Salje, E.R. Vance, S.J. Zinkle, Radiation effects in crystalline ceramics for the immobilization of high-level nuclear waste and plutonium, J. Mater. Res. 13 (1998)1434-1484.

[17] R.C. Ewing, W.J. Weber, F.W. Clinard, Radiation effects in nuclear waste forms, Prog. Nucl. Energy 29 (1995) 63-127.

[18] D.J. Gregg, E.R. Vance, Synroc tailored waste forms for actinide immobilization, Radiochim. Acta 105 (2016) 907-925.

[19] P.J. Hayward, The use of glass ceramics for immobilising high level wastes from nuclear fuel recycling, Glass Technol. 29 (1988) 122-136.

[20] D. Caurant, Glass-ceramics for waste immobilization, in From glass to crystal: Nucleation, growth and phase separation: from research to applications. Ed. by D.R.

Neuville, L. Cormier, D. Caurant and L. Montagne. EDP Science, Les Ulis (2017) 491-526.

[21] J.S. McCloy, A. Goel, Glass-ceramics for nuclear-waste immobilization, MRS Bull. 42 (2017) 233-238.

[22] W.J. Weber, Models and mechanisms of irradiation-induced amorphization in ceramics, Nucl. Instrum. Meth. B 166-167 (2000) 98-106.

[23] R. Bros, J. Carpena, V. Sere, A. Beltritti, Occurrence of Pu and fissiogenic REE in hydrothermal apatites from the fossil nuclear reactor 16 at Oklo (Gabon), Radiochim. Acta 74 (1996) 277-282.

[24] J. Carpena, Uranium-235 fission track annealing in minerals of the apatite group : an experimental study, in Advances in Fission - Track Geochronology, P. Van den Haute and F. De Corte Eds., Kluwer Academic Publishers, Dordrecht (1998) 81-92.

[25] K. Horie, H. Hidaka, F. Gauthier-Lafaye, Isotopic evidence for trapped fissiogenic REE and nucleogenic Pu in apatite and Pb evolution at the Oklo natural reactor, Geochim. Cosmochim. Acta 68 (2004) 115-125.

[26] S. Soulet, J. Carpéna, J. Chaumont, O. Kaitasov, M-O. Ruault, J-C Krupa, Simulation of the α-annealing effect in apatitic structures by He-ion irradiation: Influence of the silicate/phosphate ratio and of the OH^-/F^- substitution, Nucl. Instrum. Meth. B 184 (2001) 383-390.

[27] T.S. Livshits, Britholites as natural analogues of actinide matrices: Resistance to radiation damage, *Geol. Ore Deposit.* 48 (2006) 357-368.

[28] S. Soulet, J. Carpéna, J. Chaumont, J-C. Krupa, M-O. Ruault, Determination of the defect creation mechanism in the mono-silicated fluoroapatite. Disorder modeling under repository conditions, J. Nucl. Mater. 299 (2001) 227-234.

[29] C. Meis, J. D. Gale, L. Boyer, J. Carpena, D. Gosset, Theoretical study of Pu and Cs incorporation in a mono-silicate neodymium fluoroapatite $Ca_9Nd(SiO_4)(PO_4)_5F_2$, J. Phys. Chem. A 104 (2000) 5380-5387.

[30] J. Carpena, J-L. Lacout, Des apatites naturelles aux apatites synthétiques, L'Act. Chim. 2 (1997) 3-9.

[31] L. Boyer, J. Carpena, J.L. Lacout, Synthesis of phosphate-silicate apatites at atmospheric pressure, Solid State Ionics 95 (1997) 121-129.

[32] E.R. Vance, C.J. Ball, B.D. Begg, M.L. Carter , R.A. Day, G.J. Thorogood, Pu, U, and Hf incorporation in Gd silicate apatite, J. Am. Ceram. Soc. 86 (2003) 1223-1225.

[33] S. Utsunomiya, S. Yudintsev, L.M. Wang, R.C. Ewing, Ion-beam and electron-beam irradiation of synthetic britholite, J. Nucl. Mater. 322 (2003) 180-188.

[34] W.J. Weber, Radiation-induced swelling and amorphization in $Ca_2Nd_8(SiO_4)_6O_2$, Radiat. Eff. 77 (1983) 295-308.

[35] J.W. Wald, W.J. Weber, Effects of self-radiation damage on the leachability of actinide-host phases, Adv. Ceram. Nucl. Waste Manag. 8 (1984) 71-75.

[36] W.J. Weber, Alpha-decay induced amorphization in complex silicate structures, J. Am. Ceram. Soc. 76 (1993) 1729-1738.

[37] W.J. Weber, Radiation damage in a rare-earth silicate with the apatite structure, J. Am. Ceram. Soc. 65 (1982) 544-548.

[38] W.J. Weber, Radiation-induced amorphization in complex silicates, Nucl. Instrum. Meth. B 65 (1992) 88-92.

[39] W.J. Weber and R.C. Ewing, Radiation effects in crystalline oxide host phases for the immobilization of actinides, Mater. Res. Soc. Symp. Proc. 713 (2002) 443-454.

[40] W.J. Weber, R.C. Ewing, A. Meldrum, The kinetics of alpha-decay-induced amorphization in zircon and apatite containing weapons-grade plutonium or other actinides, J. Nucl. Mater. 250 (1997) 147-155.

[41] L.M. Wang, W.J. Weber, Transmission electron microscopy study of ion-beam-induced amorphization of $Ca_2La_8(SiO_4)_6O_2$, Phil. Mag. A 79 (1999) 237-253.

[42] W.J. Weber, R.K. Eby, R.C. Ewing, Accumulation of structural defects in ion-irradiated $Ca_2Nd_8(SiO_4)_6O_2$, J. Mater. Res. 6 (1991) 1334-1345.

[43] R. Devanathan, K.E. Sickafus, W.J. Weber, M. Nastasi, Effects of ionizing radiation in ceramics, J. Nucl. Mater. 253 (1998) 113-119.

[44] W.J. Weber, L.M. Wang, Effect of temperature and recoil-energy spectra on irradiation-induced amorphization in $Ca_2La_8(SiO_4)_6O_2$, Nucl. Instrum. Meth. B 91 (1994) 63-66.

[45] W.J. Weber, R.B. Greegor, Alpha irradiation effects in $Ca_2Nd_8(SiO_4)_6O_2$, Nucl. Instrum. Meth. B 46 (1990) 160- 164.

[46] J. Felsche, Rare earth silicates with the apatite structure, J. Solid State Chem. 5 (1972) 266-275.

[47] J.A. Fahey, W.J. Weber, F.J. Rotella, An X-ray and neutron powder diffraction study of the $Ca_{2+x}Nd_{8-x}(SiO_4)_6O_{2-0.5x}$ system, J. Solid State Chem. 60 (1985) 145-158.

[48] J.E.H. Sansom, D. Richings, P.R. Slater, A powder neutron diffraction study of the oxide-ion-conducting apatite-type phases, $La_{9.33}Si_6O_{26}$ and $La_8Sr_2Si_6O_{26}$, Solid State Ionics 139 (2001) 205-210.

[49] I. Bardez, D. Caurant, J-L. Dussossoy, P. Loiseau, C. Gervais, F. Ribot, D. R. Neuville, N. Baffier, C. Fillet, Development and characterization of rare earth-rich

glassy matrices envisaged for the immobilization of concentrated nuclear waste solutions, Nucl. Sci. Eng. 153 (2006) 272-284.

[50] I. Bardez, D. Caurant, P. Loiseau, N. Baffier, J-L. Dussossoy, C. Gervais, F. Ribot, D.R. Neuville, Structural characterization of rare earth rich glasses for nuclear waste immobilization, Phys. Chem. Glasses 46 (2005) 320-329.

[51] A. Quintas, O. Majérus, D. Caurant, J-L. Dussossoy, P. Vermaut, Crystallization of a rare-earth rich aluminoborosilicate glass with varying CaO/Na_2O ratio, J. Am. Ceram. Soc. 90 (2007) 712-719.

[52] A. Quintas, D. Caurant, O. Majérus, J-L. Dussossoy, T. Charpentier, Effect of changing the rare earth cation type on the structure and crystallization behavior of an aluminoborosilicate glass, Phys. Chem. Glasses: Eur. J. Glass. Sci. Techn. B 49 (2008) 192-197.

[53] D. Caurant, O. Majérus, P. Loiseau, I. Bardez, N. Baffier, J.L. Dussossoy, Crystallization of neodymium-rich phases in silicate glasses, J. Nucl. Mater. 354 (2006) 143-162.

[54] N. Chouard, D. Caurant, O. Majérus, J-L. Dussossoy, A. Ledieu, S. Peuget, R. Baddour-Hadjean, J-P. Pereira-Ramos, Effect of neodymium oxide on the solubility of MoO_3 in an aluminoborosilicate glass, J. Non-Cryst. Solids 357 (2011) 2752-2762.

[55] N. Chouard, D. Caurant, O. Majérus, N. Guezi-Hasni, J-L. Dussossoy, R. Baddour-Hadjean, J-P. Pereira-Ramos, Thermal stability of SiO_2-B_2O_3-Al_2O_3-Na_2O-CaO glasses with high Nd_2O_3 and MoO_3 concentrations, J. Alloys Compds. 671 (2016) 84-99.

[56] W.J. Weber, R.P. Turcotte, L.R. Bunnell, F.P. Roberts and J.H. Westsik, Radiation effects in vitreous and devitrified simulated waste glass, in Ceramics in Nuclear Waste

Management, Eds. T. D. Chikalla and J. E. Mendel, CONF-790420 (National Technical Information Service, Springfield, VA, 1979) 294-299.

[57] M.V. Swain, A fracture mechanics description of the microcracking about NiS inclusions in glass, J. Non-Cryst. Solids 38-39 (1980) 451-456.

[58] D. Zhao, L. Li, L.L. Davis, W.J. Weber and R.C. Ewing, Gadolinium borosilicate glass-bonded Gd-silicate apatite: A glass-ceramic nuclear waste form for actinides, Mater. Res. Soc. Symp. Proc. 663 (2001) 199-206.

[59] N. Chouard, D. Caurant, O. Majérus, J-L. Dussossoy, S. Klimin, D. Pytalev, R. Baddour-Hadjean, J-P. Pereira-Ramos, Effect of MoO_3, Nd_2O_3 and RuO_2 on the crystallization of soda-lime aluminoborosilicate glasses, J. Mater. Sci. 50 (2015) 219-241.

[60] A. Karamanov, Granite like materials from hazardous wastes obtained by sintercrystallisation of glass frits, Adv. Appl. Ceram. 108 (2009) 14-21.

[61] A. H. Mir, I. Monnet, M. Toulemonde, S. Bouffard, C. Jégou, S. Peuget, Mono and sequential ion irradiation induced damage formation and damage recovery in oxide glasses : stopping power dependence of the mechanical properties, J. Nucl. Mater. 469 (2016) 244-250.

[62] J. Jensen, A. Razpet, M. Skupinski, G. Possnert, Ion tracks in amorphous SiO_2 irradiated with low and high energy heavy ions, Nucl. Instrum. Meth. B 245 (2006) 269-273.

[63] J. Jensen, A. Razpet, M. Skupinski, G. Possnert, Ion track formation below 1 MeV/u in thin films of amorphous SiO_2, Nucl. Instrum. Meth. B 243 (2006) 119-126.

[64] S. Moll, L. Thomé, L. Vincent, F. Garrido, G. Sattonnay, T. Thomé, J. Jagielsky, J. M. Costantini, Damage induced by electronic excitation in ion-irradiated yttria-stabilized zirconia, J. Appl. Phys. 105 (2009) 023512.

[65] V. Picot, X. Deschanels, S. Peuget, B. Glorieux, A. M. Seydoux-Guillaume, R. Wirth, Ion beam radiation effects in monazite, J. Nucl. Mater. 381 (2008) 290-296.

[66] D.A. Long, Raman Spectroscopy, McGraw-Hill, New-York (1977).

[67] M. Toumi, L. Smiri-Dogguy, A. Bulou, Structure cristalline et spectres Raman polarisés de $Na_{1,5}Sm_{8,5}(SiO_4)_6FO$, Ann. Chim. Sci. Mat. 27 (2002) 17-26.

[68] E. Rodriguez-Reyna, A.F. Fuentes, M. Maczka, J. Hanuza, K. Boulahya, U. Amador, Structural, microstructural and vibrational characterization of apatite-type lanthanum silicates prepared by mechanical milling, *J.* Solid State Chem. 179 (2006) 522-531.

[69] L. Nasdala, R.T. Pidgeon, D. Wolf, Heterogeneous metamictization of zircon on a microscale, Geochim. Cosmochim. Acta 60 (1996) 1091-1097.

[70] L. Nasdala, R.T. Pidgeon, D. Wolf, G. Irmer, Metamictization and U-PB isotopic discordance in single zircons: a combined Raman microprobe and SHRIMP ion probe study, *Mi*neral. Petrol. 62 (1998) 1-27.

[71] M. Zhang, E.K.H. Salje, I. Farnan, A. Graeme-Barber, P. Daniel, R.C. Ewing, A.M. Clark, H. Leroux, Metamictization of zircon: Raman spectroscopic study, J. Phys. Condens. Matter 12 (2000) 1915-1925.

[72] C.S. Palenik, L. Nasdala, R.C. Ewing, Radiation damage in zircon, Am. Mineral. 88 (2003) 770-781.

[73] L. Nasdala, J.M. Hanchar, A. Kronz, M.J. Whitehouse, Long-term stability of alpha particle damage in natural zircon, Chem. Geol. 220 (2005) 83-103.

[74] K. Horie, H. Hidaka, F. Gauthier-Lafaye, Elemental distribution in zircon: alteration and radiation-damage effects, Phys. Chem. Earth 31 (2006) 587-592.

[75] W.J. Weber, R.C. Ewing, C.A. Angell, G.W. Arnold, A.N. Cormack, J-M. Delaye, D.L. Griscom, L.W. Hobbs, A. Navrotsky, D.L. Price, A.M. Stoneham, M.C. Weinberg, Radiation effects in glasses used for immobilization of high-level waste and plutonium disposition, J. Mater. Res. 12 (1997) 1948-1978.

[76] S. Peuget, P-Y. Noël, J-L. Loubet, S. Pavan, P. Nivet, A. Chenet, Effects of deposited nuclear and electronic energy on the hardness of R7T7-type containment glass, Nucl. Instrum. Meth. B 246 (2006) 379-386.

[77] S. Peuget, J-M. Delaye, C. Jégou, Specific outcomes of the research on the radiation stability of the French nuclear glass towards alpha decay accumulation, J. Nucl. Mater. 444 (2014) 76-91.

[78] S. Peuget, J-N. Cachia, C. Jégou, X. Deschanels, D. Roudil, V. Broudic, J-M. Delaye, J.M. Bart, Irradiation stability of R7T7-type borosilicate glass, J. Nucl. Mater. 354 (2006) 1-13.

[79] J. De Bonfils, S. Peuget, G. Panczer, D. De Ligny, S. Henry, P.Y. Noel, A. Chenet, B. Champagnon, Effect of chemical composition on borosilicate glass behavior under irradiation, J. Non-Cryst. Solids 356 (2010) 388-393.

[80] S. Peuget, C. Mendoza, E.A. Maugeri, J.M. Delaye, R. Caraballo, T. Charpentier, M. Tribet, O. Bouty, C. Jégou, Alpha decays impact on nuclear glass structure, Proc. Mater. Sci. 7 (2014) 252-261.

[81] G. Bureau, J-M. Delaye, S. Peuget, G. Calas, Molecular dynamics study of structural changes versus deposited energy dose in a sodium borosilicate glass, Nucl. Instrum. Meth. B 266 (2008) 2707-2710.

[82] D.R. Neuville, Viscosity, structure and mixing in (Ca, Na) silicate melts, Chem. Geol. 229 (2006) 28-41.

[83] W.L. Konijnendijk, J. M. Stevels, The structure of borosilicate glasses studied by Raman scattering, J. Non-Cryst. Solids 20 (1976) 193-224.

[84] C. Mendoza, S. Peuget, O. Bouty, R. Caraballo, C. Jegou, Simplified nuclear glasses structure behaviour under various irradiation conditions: a Raman spectroscopy study, Proc. Chem. 7 (2012) 581-586.

[85] T. Charpentier, L. Martel, A.Mir, J. Somers, C. Jégou, S. Peuget, Self-healing capacity of nuclear glass observed by NMR spectroscopy, Scientific Reports, Nature Publishing Group, 6 (2016) 25499.

[86] A. Quintas, O. Majérus, M. Lenoir, D. Caurant, K. Klementiev, A. Webb, Effect of alkali and alkaline-earth cations on the neodymium environment in a rare-earth rich aluminoborosilicate glass, J. Non-Cryst. Solids. 354 (2008) 98-104.

[87] W.J. Weber, R-P. Turcotte, L.R. Bunnel, F.P. Roberts, J.H. Westsik, Radiation effects in vitreous and devitrified simulated waste glass, in Ceramics in Nuclear Waste Management, Eds. T.D. Chikalla and J.E. Mendel, CONF-790420 (National Information Service, Springfield, VA, 1979) p. 294.

[88] E. Snoeks, A. Polaman, C.A. Volkert, Densification, anisotropic deformation, and plastic flow of SiO_2 during MeV heavy ion irradiation, Appl. Phys. Lett. 65 (1994) 2487-2489.

[89] A.I. Ryazanov, H. Trinkaus, A.E. Volkov, Incubation dose for ion beam induced anisotropic growth of amorphous alloys: Insight into amorphous state modifications, Phys. Rev. Lett. 84 (2000) 919-922.

[90] A. Benyagoub, S. Löffler, M. Rammensec, S. Klaumünzer, G. Saemann-Ischenko, Plastic deformation in SiO_2 induced by heavy-ion irradiation, Nucl. Instrum. Meth. B 65 (1992) 228-231.

[91] H. Trinkaus, Local stress relaxation in thermal spikes as a possible cause for creep and macroscopic stress relaxation of amorphous solids under irradiation, J. Nucl. Mater. 223 (1995) 196-201.

[92] H. Trinkaus, Dynamics of viscoelastic flow in ion tracks: origin of plastic deformation of amorphous materials, Nucl. Instrum. Meth. B 146 (1998) 204-216.

Glass	SiO_2	B_2O_3	Al_2O_3	Na_2O	CaO	Nd_2O_3
PG	56.78	10.24	5.00	16.16	8.23	3.59
RG	59.06	8.10	6.05	17.11	7.44	2.24

Table 1. Nominal composition (in mol%) of the parent glass (PG) synthesized for the preparation of the glass-ceramics and of the residual glass (RG) prepared for irradiation experiments. The composition of RG glass was determined after analysis by EPMA (Electron Probe Micro-Analysis) of the residual glass in the glass-ceramic samples. The apparent decrease of B_2O_3 content (~ 2 mol%) in RG glass in comparison with PG glass cannot be explained by a partitioning of boron in the apatite crystals of the glass-ceramic (EPMA did not reveal any trace of boron in the crystals) but rather to the difficulty to correctly analyze boron by EPMA in the glass (existence of a large variation of B_2O_3 content for the different point analysis).

	Ion	Energy (MeV)	R_p (µm)	S_n (keV/nm)	S_e (keV/nm)
Ceramic	Au	1.9-6.75	1.1	2.8	3.0
	Xe	90	9	0.164	17.5
	Xe	995	47	0.022	24.2
	Ar	35	7	0.017	6.9
	RN	0.1	0.026	2.5	0.3
	AP	5	15.5	< 0.02	0.35
Glass	Au	1.9-6.75	1.7	2.0	2.6
	Xe	90	11	0.011	13.9
	Xe	995	61	0.015	17.5
	Ar	35	9	0.012	5.4
	RN	0.1	0.036	2.0	0.25
	AP	5	19.5	<0.03	0.3

Table 2. Irradiation parameters for the $Ca_2Nd_8(SiO_4)_6O_2$ apatite and the RG glass irradiated with 1.9 - 6.75 MeV Au ions (ME irradiations), 90 or 995 MeV Xe ions and 35 MeV Ar ions (SHI irradiations). The values of S_n and S_e (respectively the nuclear and electronic stopping powers) correspond to the values obtained over the first nm of the irradiated depth (SRIM simulations). R_p is the projected ion range. It is worth noting that in reality, the S_e values progressively decreases along the irradiated depth (for ME and 90 MeV SHI irradiations) whereas the S_n values are almost constant (except at the end of the ion path for SHI irradiations, due to recoil nuclei) (see Fig. 4). For

comparison, the stopping power of an α-particle (AP) of 5 MeV and a recoil nucleus (RN, uranium) coming from an α-decay are also presented (SRIM simulations).

Site	Nd number	CN	Mean Nd-O (Å)	Nd-O standard dev. (Å^2)
4f	2.2	9	2.57	0.017
6h	5.8	7	2.47	0.031
Average site		7.5	2.53	0.026

Table 3. Description of the 4f and 6h sites that are occupied by Nd^{3+} ions in the structure of $Ca_2Nd_8(SiO_4)_6O_2$ apatite according to the ICDD 00-28-2287 file: Nd number is the site occupancy by Nd^{3+}, CN is the site coordination number. From these two parameters, an average site is calculated for Nd^{3+} in the $Ca_2Nd_8(SiO_4)_6O_2$ apatite with an average CN, a mean Nd-O distance and a Nd-O standard deviation. These 3 structural parameters serve as a reference for the fit of the non-irradiated $Ca_2Nd_8(SiO_4)_6O_2$ ceramic (first shell component in the EXAFS signal), in order to check the phase and amplitude parameters of the Nd-O single scattering function and determine the S_0^2 and ΔE_0 values to be used in the fits.

	ΔE_0 (eV)	S_0^2	CN	Nd-O (Å)	σ^2 (Å^2) and cumulants
Path 1	5	0.95	3	2.44	0.018 cum3 = 0 Å^3, cum4 = 0 Å^4
Path 2	-10	0.95	5	2.59	0.044 cum3 = 0.00463 Å^3 cum4 = 0.00099 Å^4
Average			8	2.53	

Table 4. Results of the fit of the Nd-O shell in non-irradiated $Ca_2Nd_8(SiO_4)_6O_2$ ceramic, using single scattering phase and amplitude calculated by FEFF6 (path 1 : d(Nd-O) = 2.46 Å and path 2 : d(Nd-O) = 2.53 Å). Fit quality numbers were reduced-χ^2 = 25.7 and R-factor = 0.0064.

Irradiation	CN	Nd-O ± 0.03 Å	σ^2 ± 0.006 Å^2	Cum3 (Å^3) ± 0.0009 Å^3	Cum4 (Å^4) ± 0.0003 Å^4	R-factor
			Apatite ceramic			
ME-F1	6	2.51	0.050	0.0021	0.0013	0.018
ME-F2	6	2.50	0.051	0.0012	0.0013	0.020
SHI	6	2.50	0.047	0.0015	0.0012	0.024
			RG glass			
Pristine	6	2.45	0.025	0.0013	0.0006	0.0016
ME-F1	6	2.45	0.032	0.0016	0.0007	0.0036
ME-F3	6	2.45	0.031	0.0021	0.0005	0.0308
SHI	6	2.45	0.034	0.0015	0.0009	0.0038

Table 5. Structural parameters of the Nd-O first shell in the irradiated apatite ceramic and RG glass samples deduced from the fit of the Fourier transform of the $k^3.\chi(k)$ signals (Figs. 11a and 11b). The coordination number CN was fixed in the fits. ME irradiation: 1.9 - 6.75 MeV Au ions (F1 = 3.11×10^{13}, F2 = 6.22×10^{13}, F3 = 1.24×10^{14} ions/cm^2). SHI irradiation: 35 MeV Ar ions (fluence 2×10^{13} ions/cm^2). The structural parameters of pristine RG glass are also given in the Table.

	ME irradiation	**SHI irradiation**
Swelling	8 %	5 %
Hardness variation	-37 %	-37.5%
Amorphization	Yes	Yes
Raman vibration band position *(initial position : 862 cm^{-1})*	846 cm^{-1}	840 cm^{-1}
Raman vibration band FWHM *(initial FWHM : 13 cm^{-1})*	50 cm^{-1}	45 cm^{-1}
Average Nd-O distance *(initial average distance: 2.53 Å)*	2.50-2.51 Å	2.50 Å
σ^2 *(initial σ^2: 0.026 $Å^2$)*	0.050-0.051 $Å^2$	0.047 $Å^2$

Table 6. Comparison of the macroscopic and structural modifications induced by ME (1.9 - 6.75 MeV Au ions) and SHI (90 MeV Xe ions or 35 MeV Ar ions) irradiations in the $Ca_2Nd_8(SiO_4)_6O_2$ apatite ceramic. The data given in italics are those of the pristine apatite ceramic.

	ME irradiation	**SHI irradiation**
Swelling	~1 %	~0.2-0.5%
Hardness variation	-33 %	-33.5%
Average Nd-O distance *(initial average distance: 2.45 Å)*	2.45 Å	2.45 Å
σ^2 *(initial σ^2: 0.025)*	0.031-0.032 Å^2	0.034 Å^2
Cum3 *(initial:0.0013 Å^3)*	0.0016-0.0021 Å^3	0.0015 Å^3

Table 7. Comparison of the macroscopic and structural modifications induced by ME (1.9 - 6.75 MeV Au ions) and SHI (90 MeV Xe ions or 35 MeV Ar ions) irradiations in RG glass. The data given in italics are those of pristine RG glass.

Figure captions

Figure 1. Scheme showing the risks of crack formation in the bulk of a partially crystallized nuclear waste glass during storage (only two crystals (in purple) containing actinides are shown in the figure). Cracks (in black) may be induced in the residual glass (in grey) by the amorphization + swelling under α self-irradiation of the crystals containing actinides: (a) at the beginning of storage, (b) after a long period of storage (accumulation of α-decays in the crystals containing actinides and increase of strains in the residual glass in their neighborhood).

Figure 2. Scheme comparing the irradiation depth induced by ME (1.9 - 6.75 MeV Au) heavy ions (a) and SHI (995 MeV Xe) heavy ions (b) in a glass-ceramic sample containing apatite crystals (in purple).

Figure 3. SEM images (back-scattered electrons) of the glass ceramics GCA (a) and GCB (b).

Figure 4. Electronic (red) and nuclear (blue) energy losses in the $Ca_2Nd_8(SiO_4)_6O_2$ apatite versus ion energy, for 6.75 MeV Au ions (a), 90 MeV Xe ions (b) and 995 MeV Xe ions (c) calculated by the SRIM code. For Au ions irradiation (a) the nuclear energy loss is significant all along the ion path contrary to the Xe high energy irradiations for which the electronic energy loss largely dominates (b,c). In the case of Au ions irradiation, the use of two energies (1.9 and 6.75 MeV) was perform to obtain a ballistic

damage almost constant all along the irradiated depth (d), with a dpa value of around 3.7 in the first 1.2µm for an irradiation fluence of $9.47x10^{14}$ ions.cm^{-2}.

Figure 5. (a) Optical micrograph of the interface (I) between the irradiated area (left side) and the pristine area (right side) of the $Ca_2Nd_8(SiO_4)_6O_2$ apatite ceramic sample irradiated with 90 MeV Xe ions (2×10^{13} ions/cm^2). (b) Step height profile. The insert shown in (b) is a picture of the irradiated ceramic with the masked region on its right.

Figure 6. Swelling measurement of the $Ca_2Nd_8(SiO_4)_6O_2$ apatite ceramic irradiated with 1.9 - 6.75 MeV Au ions (black squares) and with 90 MeV Xe ions (white circles) as a function of the irradiation fluence.

Figure 7. Vickers hardness variation of the $Ca_2Nd_8(SiO_4)_6O_2$ apatite ceramic irradiated with 1.9 - 6.75 MeV Au ions (ME irradiations, black squares) and with 90 MeV Xe ions (SHI irradiations, white circles), as a function of the irradiation fluence. The 0 in the Y scale correspond to the value of the initial hardness of pristine apatite ceramic.

Figure 8. XRD patterns of the $Ca_2Nd_8(SiO_4)_6O_2$ apatite ceramic before and after irradiation at different fluences with ME (1.9 - 6.75 MeV Au ions) (a) and SHI (90 MeV Xe ions) (b) irradiations. For ME irradiations, XRD patterns were recorded in grazing incidence mode whereas for SHI irradiations, XRD patterns were recorded in standard θ-2θ geometry. F0 reference corresponds to the XRD pattern of the pristine ceramic apatite. For ME irradiations, the total fluences are F1 = 3.11×10^{13}, F2 =

6.22×10^{13}, F3 = 1.24×10^{14}, F4 = 2.18×10^{14}, F5 = 3.11×10^{14} and F6 = 9.47×10^{14} Au/cm^2. For SHI irradiations, f1 = 2×10^{11}, f2 = 2×10^{13} and f3 = 1×10^{14} Xe/cm^2.

Figure 9. Normalized Raman spectra of the apatite ceramic $Ca_2Nd_8(SiO_4)_6O_2$ before and after irradiation at different fluences with ME (1.9 - 6.75 MeV Au ions) (a) and SHI (90 MeV Xe ions) (b) irradiations. F0 reference corresponds to the Raman spectrum of the pristine ceramic apatite. For LE irradiations, F1 = 3.11×10^{13}, F2 = 6.22×10^{13}, F3 = 1.24×10^{14}, F4 = 2.18×10^{14}, F5 = 3.11×10^{14} and F6 = 9.47×10^{14} Au/cm^2. For SHI irradiations, f1 = 2×10^{11}, f2 = 2×10^{13} and f3 = 1×10^{14} Xe/cm^2.

Figure 10. (a) Example of simulation of a Raman spectrum (750-1050 cm^{-1} region) of the $Ca_2Nd_8(SiO_4)_6O_2$ apatite ceramic irradiated with 1.9 - 6.75 MeV Au ions ($1.24\text{x}10^{14}$ ions/cm^2, F3 in Fig. 9a). This region of the spectrum corresponds to the stretching vibration bands of SiO_4 (Q^0) entities. The band on the left is induced by irradiation (Fig. 9a). *: Vibration band whose position remains identical in the pristine and irradiated ceramics but whose full width at half maximum (FWHM) increases after irradiation. (b) Evolution of the full width at half maximum (FWHM) of the Raman vibration band of maximum intensity (initially located at 862 cm^{-1} in the pristine $Ca_2Nd_8(SiO_4)_6O_2$ apatite ceramic, Fig. 9) corresponding to vibrations of the SiO_4 (Q^0) units in samples irradiated with 1.9 - 6.75 MeV Au ions (ME irradiations, black squares) or with 90 MeV Xe ions (SHI irradiations, white circles), as a function of the irradiation fluence.

Figure 11. a) Full lines: Fourier transforms of the $k^3.\chi(k)$ Nd-L_3 edge GI-EXAFS signal (magnitude) for the non-irradiated apatite and the irradiated apatite ceramic with ME (1.9 - 6.75 MeV Au ions, fluences are indicated in the figure in ions/cm^2) and SHI (35

MeV Ar ions; fluence: 2×10^{13} ions/cm^2) irradiations. Dots: fits of the first shell of the Fourier transforms (Nd-O). b) Idem for the non-irradiated and irradiated RG glasses. The structural parameters resulting from the fits are reported in Table 5.

Figure 12. (a) Evolution of the Raman spectrum of the $Ca_2Nd_8(SiO_4)_6O_2$ apatite ceramic with depth from the surface after irradiation with Xe ions (90 MeV, 2×10^{13} ions/cm^2). The ceramic sample was cut perpendicularly to the irradiated surface and spectra were recorded at different distances along the slice. (b) Evolution with the distance from the irradiated ceramic surface of the FMWH of the band associated with the symmetric stretching vibrations of SiO_4 (Q^0) entities (located at 862 cm^{-1} for the pristine apatite ceramic). The evolution with depth of the electronic stopping power S_e calculated by SRIM for this ceramic is given on the axis on the top of the figure. Xe ions did not penetrate above 10 µm (the band shape is not affected by irradiation above this depth) whereas between 9.5 and 7 µm a progressive increase of FMWH is observed (partial apatite amorphization). Between 0 and 6.5 µm FMWH remains high and constant (45 cm^{-1}) indicating total apatite amorphization.

Figure 13. (a) Swelling measurement of the residual glass RG irradiated with 1.9 - 6.75 MeV Au ions as a function of the irradiation fluence. Vickers hardness variation of the residual glass RG irradiated with: (b) 1.9 - 6.75 MeV Au ions (ME irradiations); (c) 90 MeV and 995 MeV Xe ions (SHI irradiations) as a function of the irradiation fluence.

Figure 14. Normalized Raman spectra of RG glass before irradiation (F0) and after irradiation (F6) with 1.9 - 6.75 MeV Au ions (9.47×10^{14} ions/cm^2): (a) 100-1600 cm^{-1} region, (b) 825-1225 cm^{-1} region.

Figure 15. Normalized Raman spectra of RG glass before irradiation and after irradiation with 90 MeV Xe ions at various fluences (2×10^{11}, 2×10^{13} and 1×10^{14} ions/cm^2): (a) 100-1600 cm^{-1} region, (b) 825-1225 cm^{-1} region.

Figure 16. XRD patterns of the surface of the glass-ceramics GCA (a) and GCB (b) before and after SHI irradiation (995 MeV Xe ions, 2×10^{13} ions/cm^2). XRD patterns were recorded in standard θ-2θ geometry. All the lines observed on the patterns are due to apatite crystals.

Figure 17. Normalized Raman spectra of the glass-ceramics GCA (a) and GCB (b) before (1) and after irradiation (2) with 995 MeV Xe ions (2×10^{13} ions/cm^2). The black circles in (b) indicate the contribution of residual glass because of the small size of apatite crystals in CGB (Figs. 3 and 18). For GCA, the crystals size (Figs. 3 and 18) enabled to probe only the apatite phase without residual glass contribution.

Figure 18. SEM images (back-scattered electrons) of the surface of the glass-ceramic GCA before (a) and after SHI irradiation (b) with Xe ions (995 MeV, fluence 2×10^{13} ions/cm^2). (c) and (d) are respectively the SEM images of the SHI irradiated GCB and GCA samples along the edge after cutting perpendicularly to the samples surface. The

white phase is apatite. The scale bars given at the bottom left of each image corresponds to 10 μm. The irradiated depth is of around 60μm.

Figure 19. Evolution of the microstructure of the surface of the glass-ceramic GCA after SHI irradiation (Xe ions 995 MeV, 2×10^{13} ions/cm^2). As the sample was partially covered by a 200μm thick aluminum fold during irradiation, two regions can be distinguished in the figures: an irradiated region (IR) on the left of the images and a non-irradiated region (NIR) on the right. (a) Optical microscopy image. The line indicated by I in the figure corresponds to the limit between the two regions. Apatite crystals (Ap) appear in white. (b) Step height profile and (c) 3D topographic profile due to swelling across the limit between the two regions obtained by optical interferometry using a red laser.

Figure 1

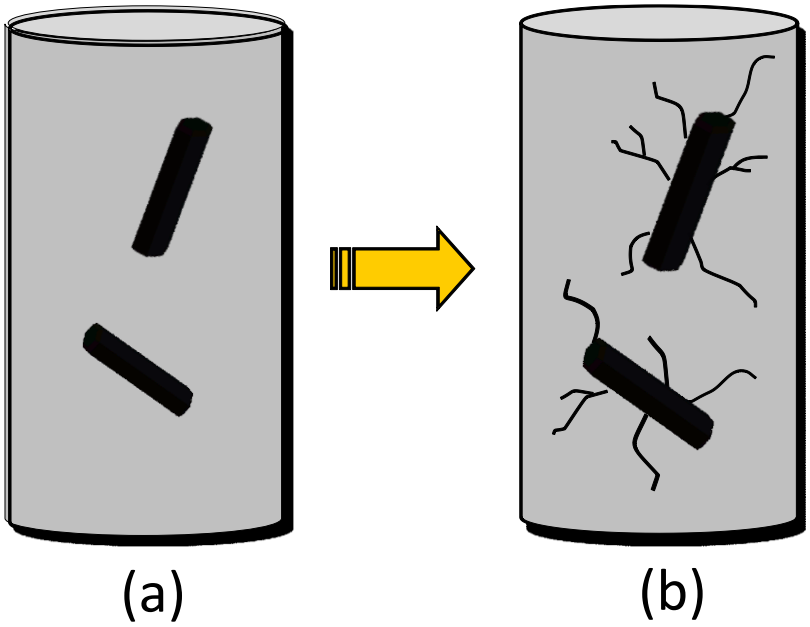

Figure 2

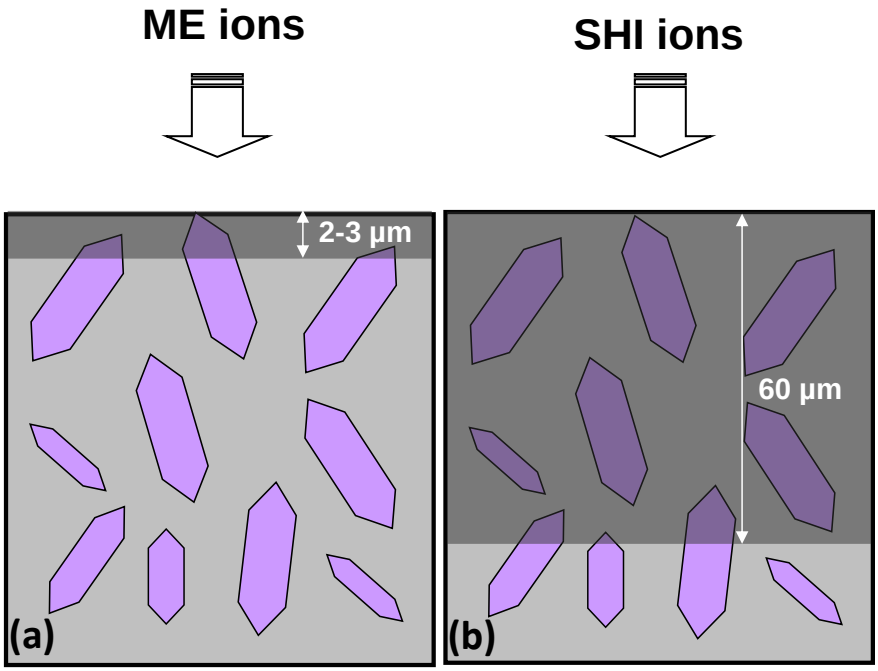

Figure 3

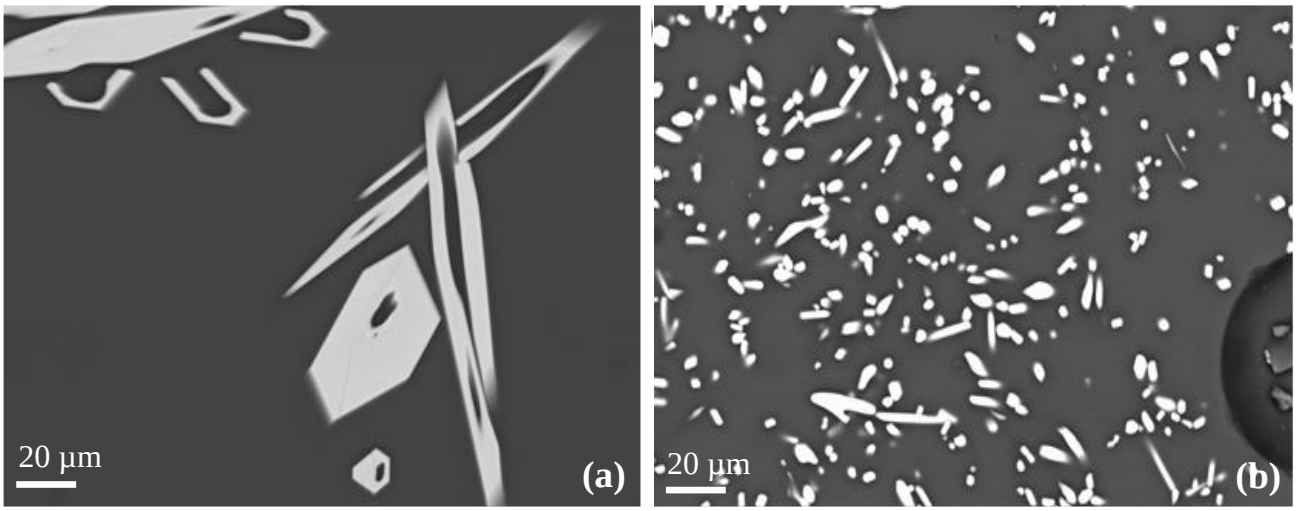

Figure 4

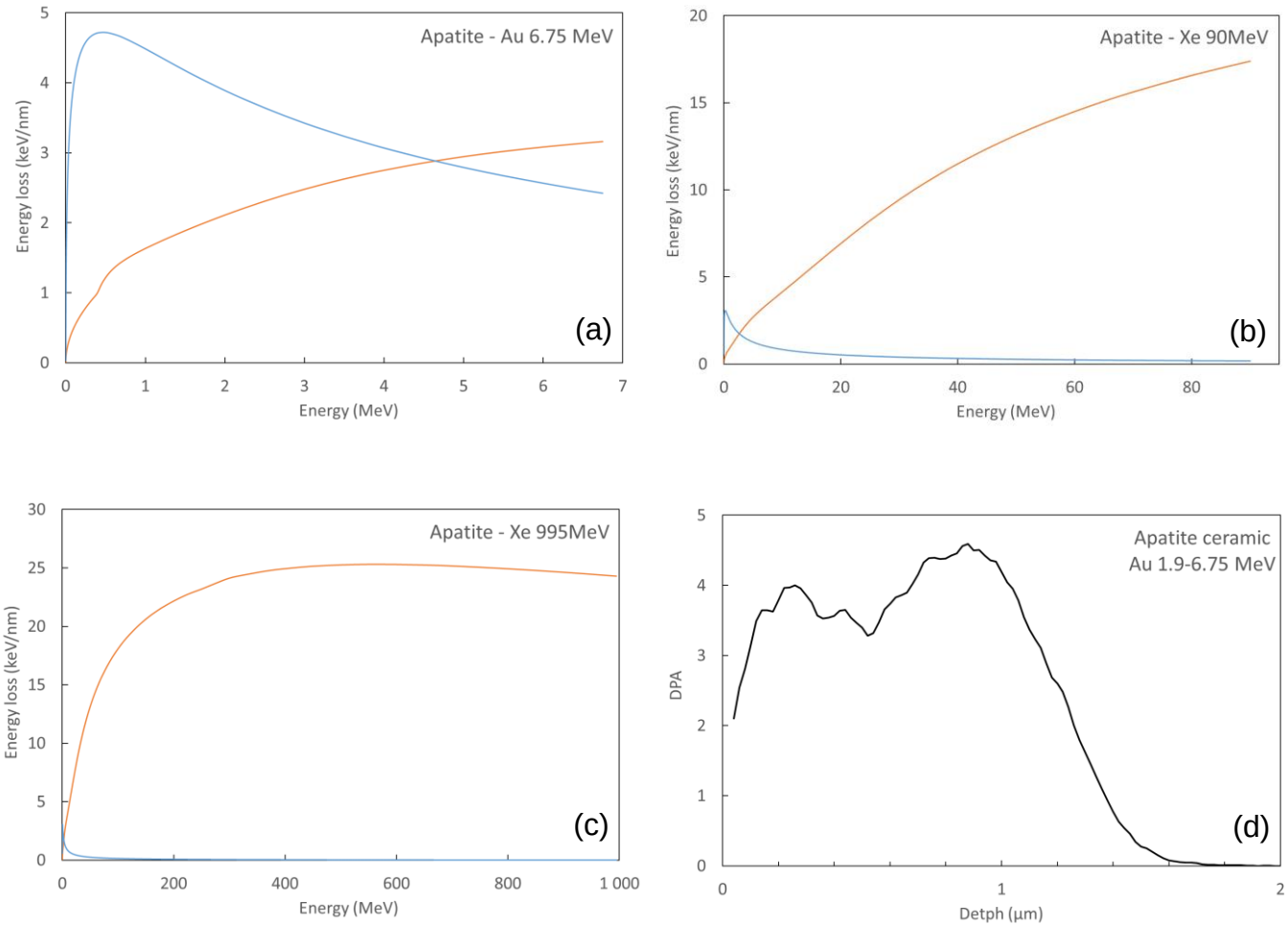
Apatite - Au 6.75 MeV
Energy loss (keV/nm)
Energy (MeV)
(a)
Apatite - Xe 90MeV
Energy loss (keV/nm)
Energy (MeV)
(b)
Apatite - Xe 995MeV
Energy loss (keV/nm)
Energy (MeV)
(c)
Apatite ceramic
Au 1.9-6.75 MeV
DPA
Detph (µm)
(d)

Figure 5

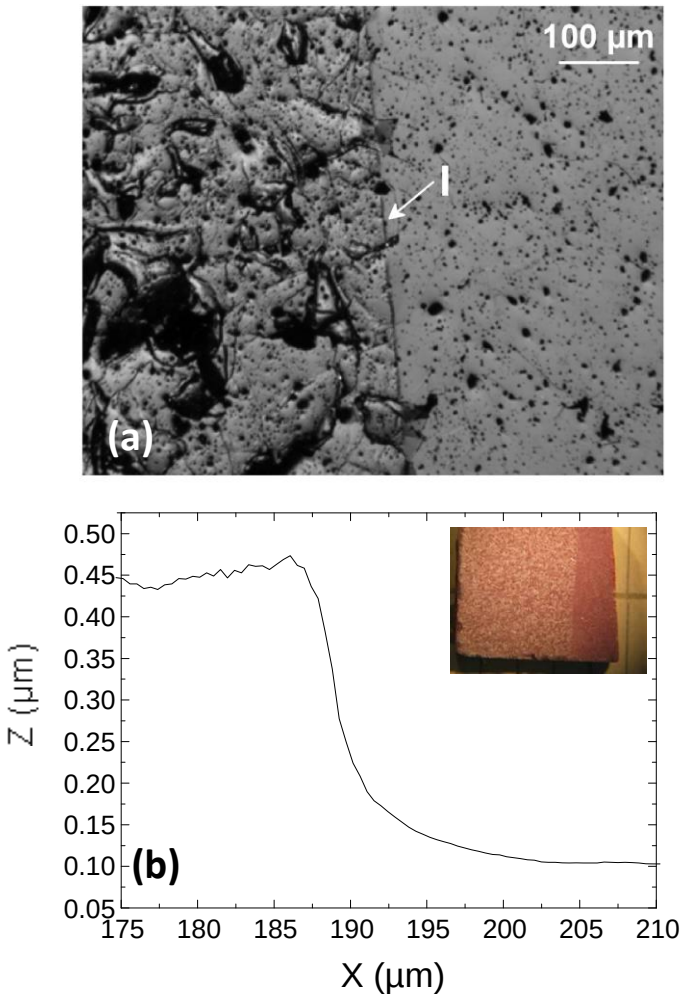
100 µm
I
(a)
0.50
0.45
0.40
0.35
0.30
0.25
0.20
0.15
0.10
0.05
Z (µm)
(b)
175
180
185
190
195
200
205
210
X (µm)

Figure 6

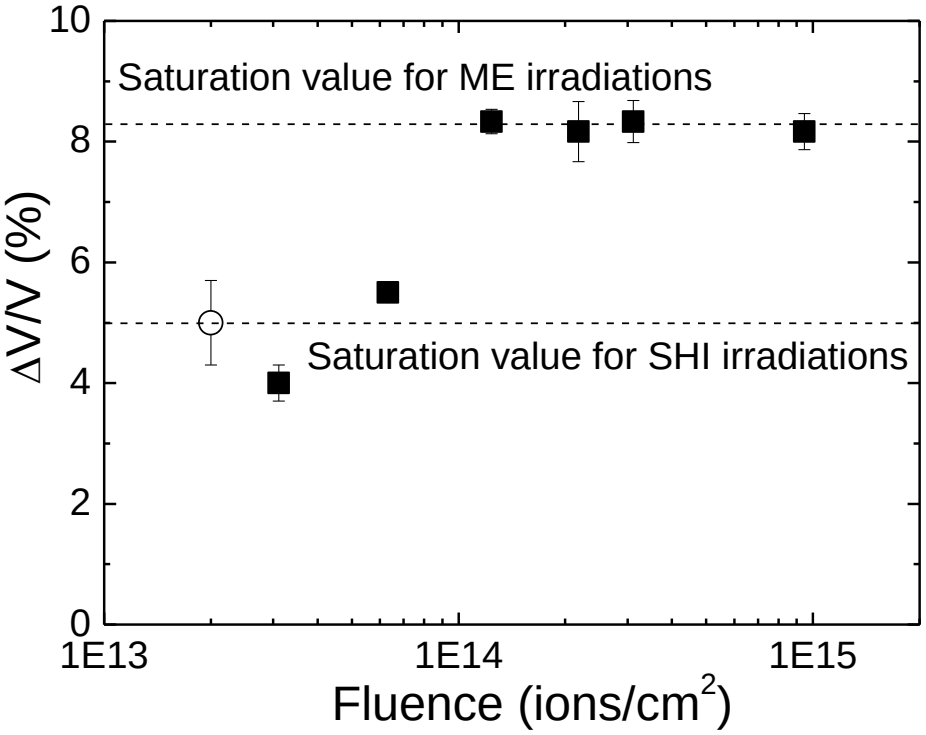
10
8
6
4
2
0
ΔV/V (%)
Saturation value for ME irradiations
Saturation value for SHI irradiations
1E13
1E14
1E15
Fluence (ions/cm2)

Figure 7

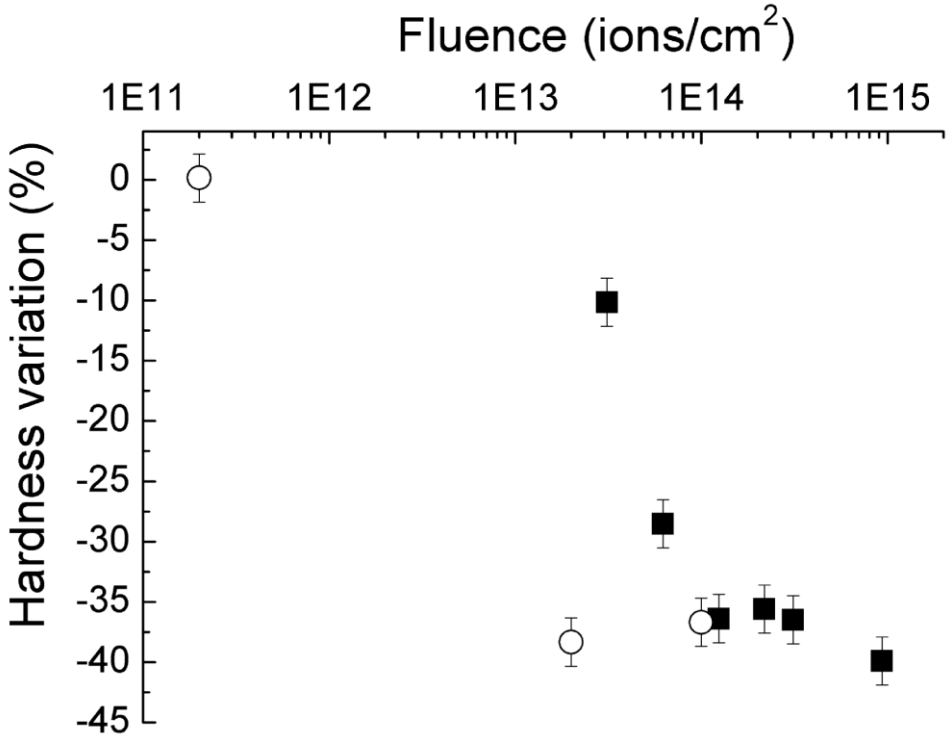
Fluence (ions/cm^2)
1E11
1E12
1E13
1E14
1E15
Hardness variation (%)
0
-5
-10
-15
-20
-25
-30
-35
-40
-45

Figure 8

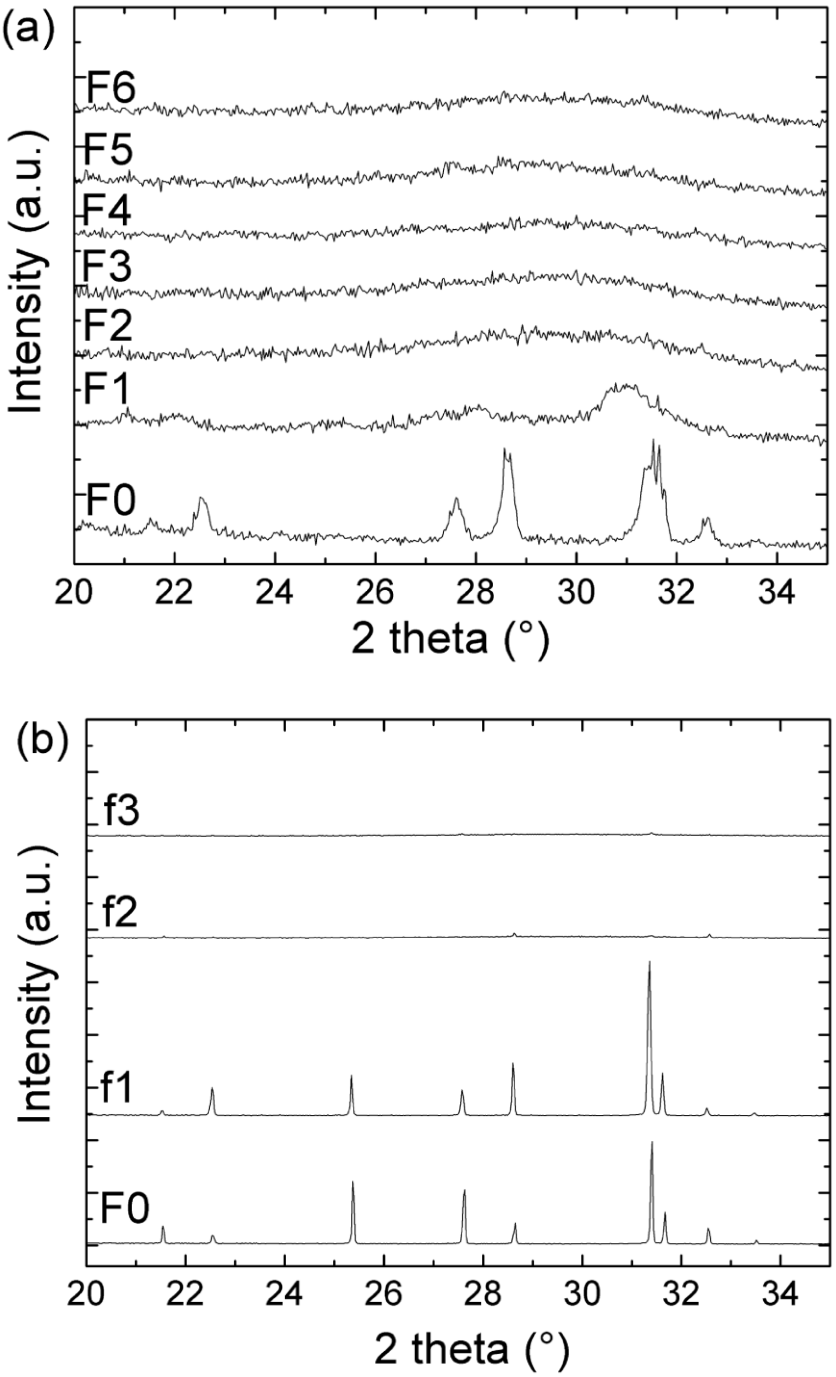
(a)
F6
F5
F4
F3
F2
F1
F0
Intensity (a.u.)
20
22
24
26
28
30
32
34
2 theta (°)
(b)
f3
f2
f1
F0
Intensity (a.u.)
20
22
24
26
28
30
32
34
2 theta (°)

Figure 9

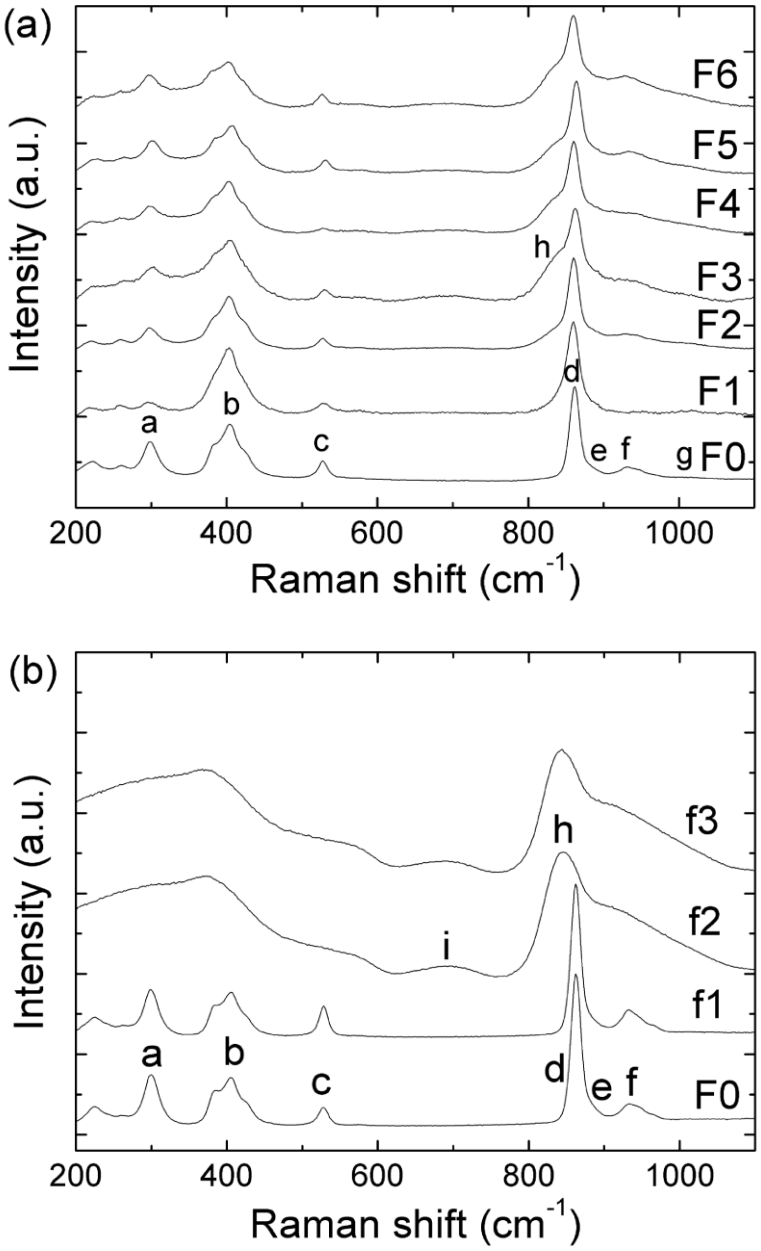
(a)
Intensity (a.u.)
F6
F5
F4
F3
F2
F1
F0
a
b
c
d
e
f
g
h
200
400
600
800
1000
Raman shift (cm-1)
(b)
Intensity (a.u.)
f3
f2
f1
F0
a
b
c
d
e
f
h
i
200
400
600
800
1000
Raman shift (cm-1)

Figure 10

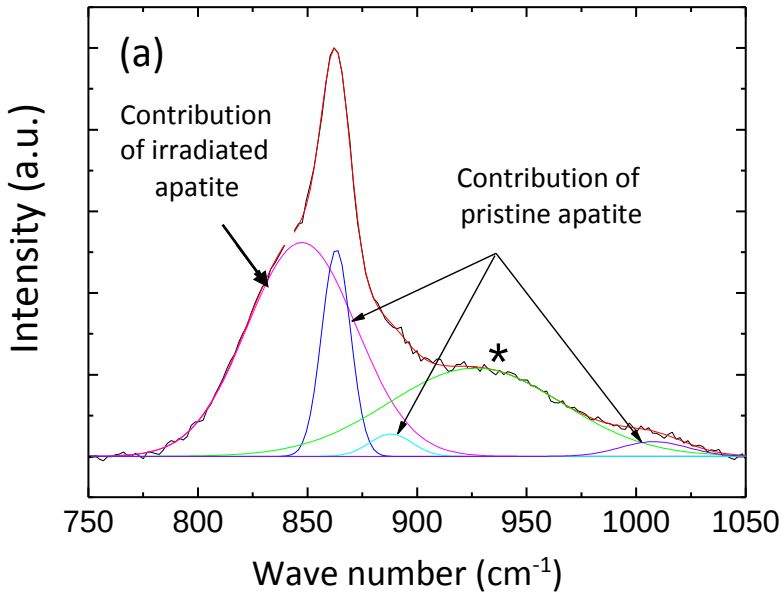
(a)
Contribution of irradiated apatite
Contribution of pristine apatite
*
Intensity (a.u.)
750
800
850
900
950
1000
1050
Wave number (cm-1)

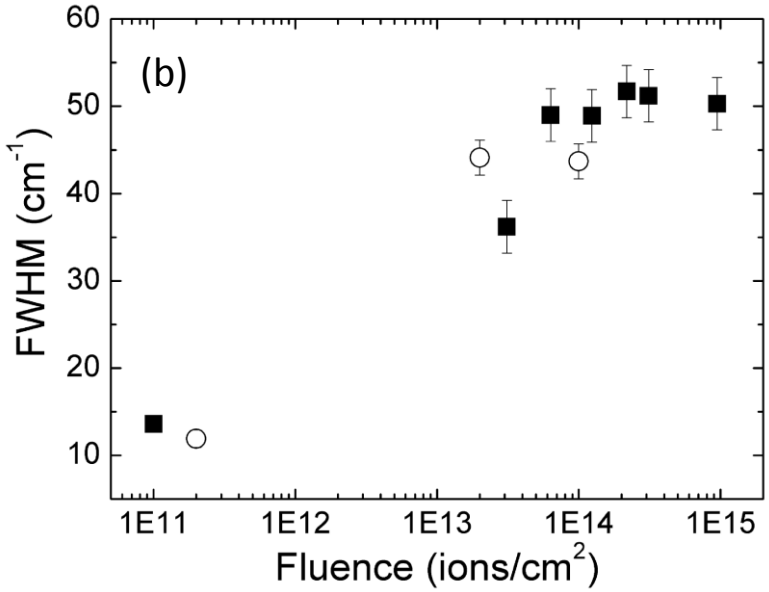
(b)
FWHM (cm-1)
60
50
40
30
20
10
1E11
1E12
1E13
1E14
1E15
Fluence (ions/cm2)

Figure 11

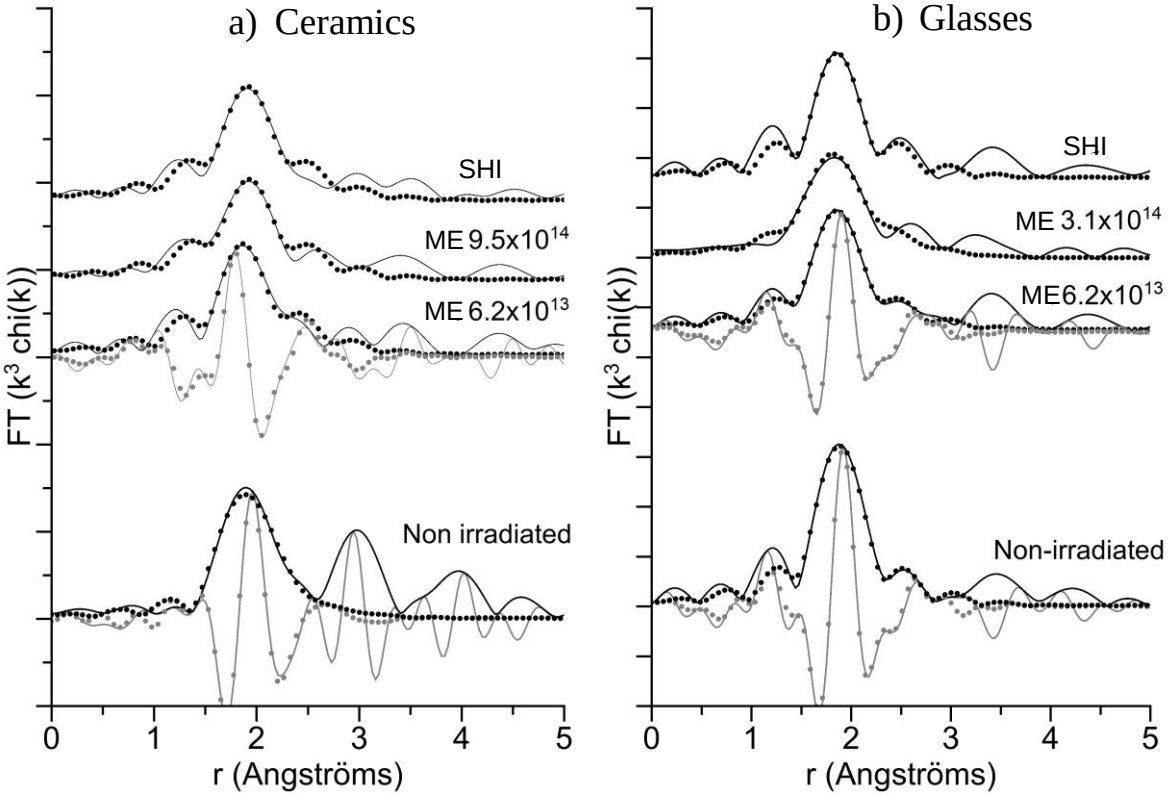
a) Ceramics
SHI
ME 9.5x10^14
ME 6.2x10^13
Non irradiated
FT (k^3 chi(k))
r (Angströms)
b) Glasses
SHI
ME 3.1x10^14
ME6.2x10^13
Non-irradiated
FT (k^3 chi(k))
r (Angströms)

Figure 12

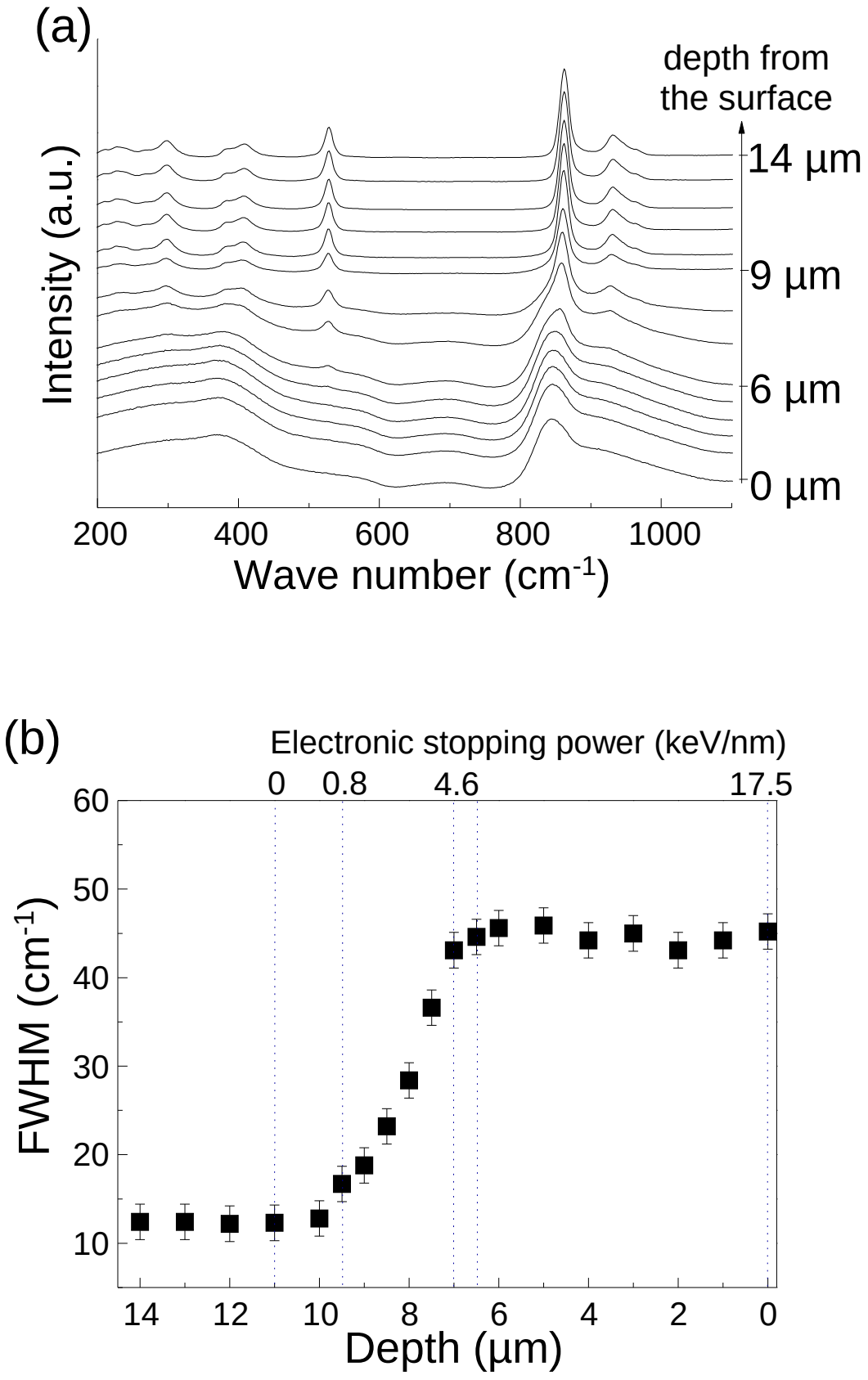
(a)
depth from
the surface
14 µm
9 µm
6 µm
0 µm
Intensity (a.u.)
200
400
600
800
1000
Wave number (cm-1)
(b)
Electronic stopping power (keV/nm)
0
0.8
4.6
17.5
FWHM (cm-1)
60
50
40
30
20
10
14
12
10
8
6
4
2
0
Depth (µm)

Figure 13

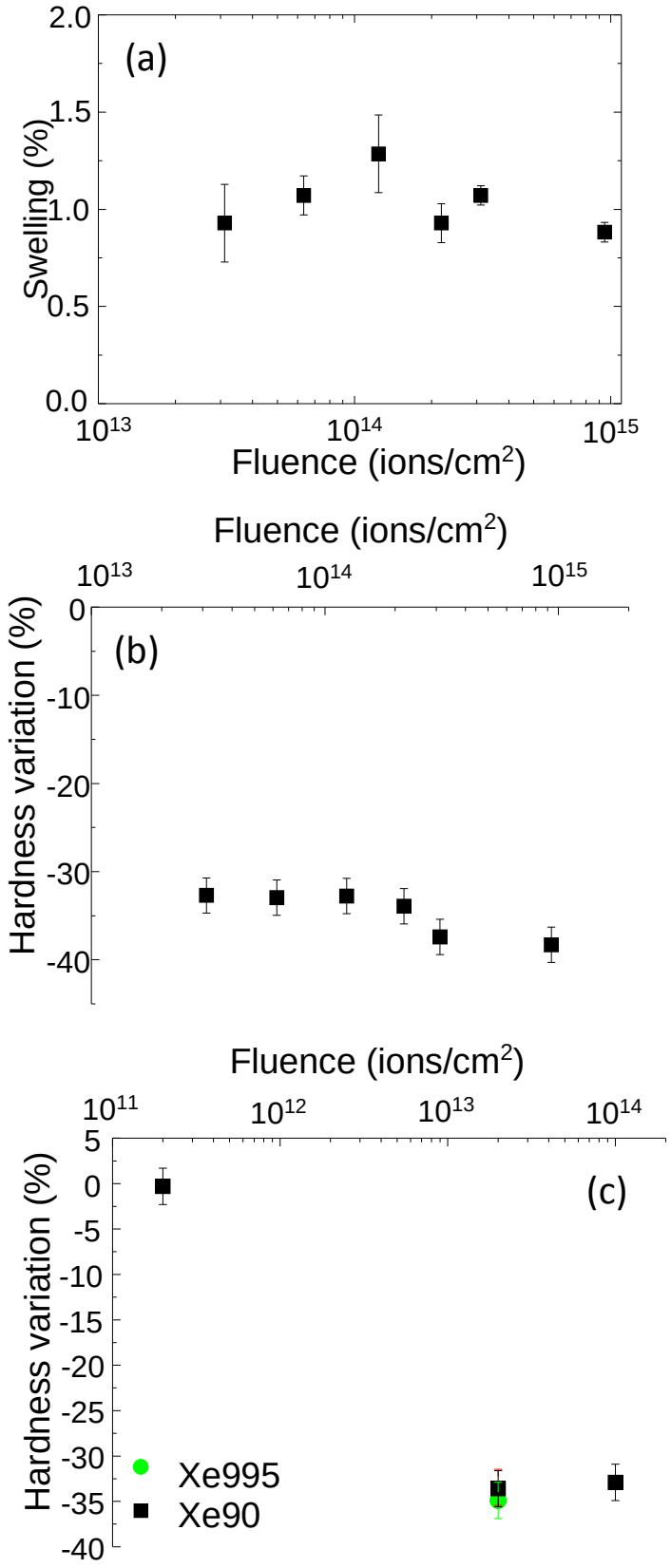
(a)
Swelling (%)
2.0
1.5
1.0
0.5
0.0
10^{13}
10^{14}
10^{15}
Fluence (ions/cm^2)
(b)
Hardness variation (%)
0
-10
-20
-30
-40
10^{13}
10^{14}
10^{15}
Fluence (ions/cm^2)
(c)
Hardness variation (%)
5
0
-5
-10
-15
-20
-25
-30
-35
-40
10^{11}
10^{12}
10^{13}
10^{14}
Fluence (ions/cm^2)
Xe995
Xe90

Figure 14

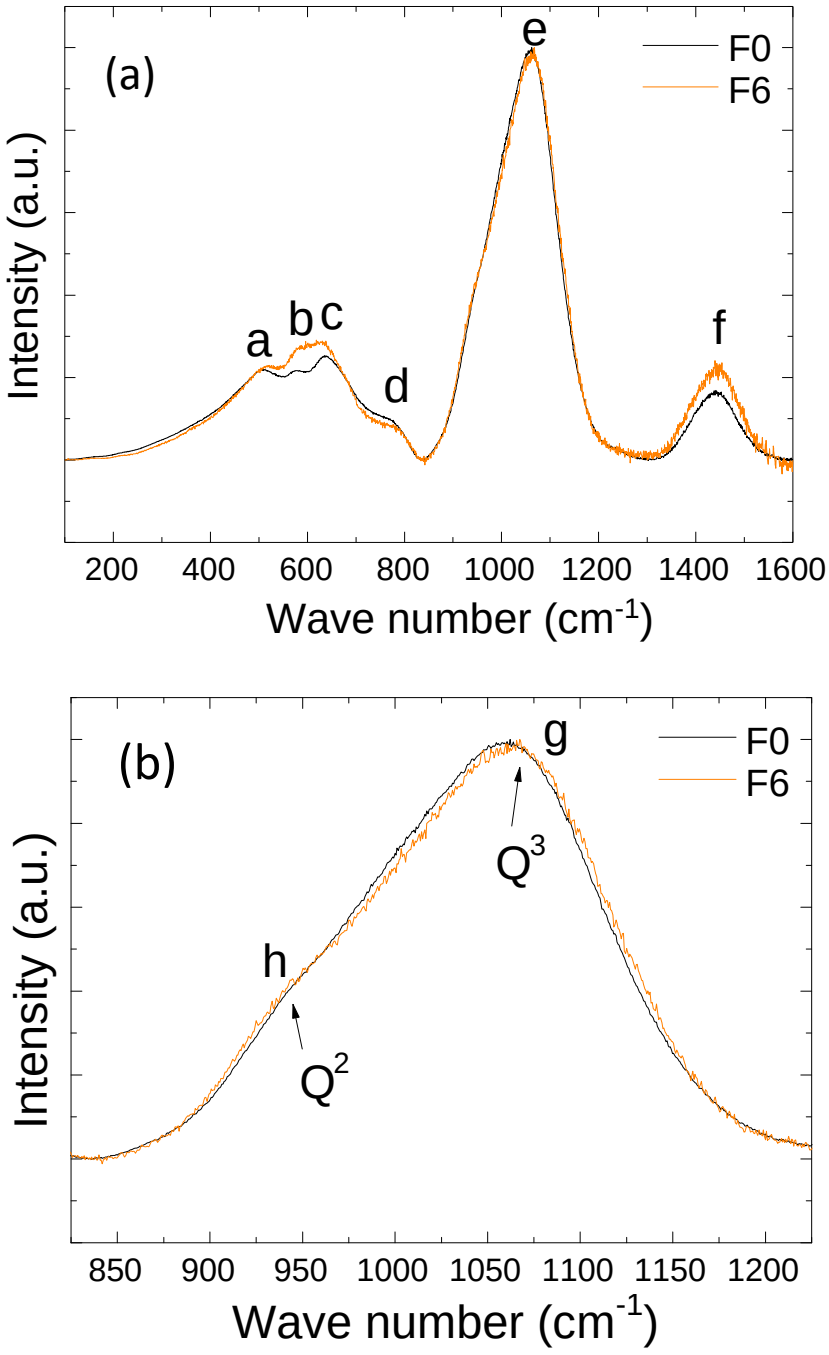
(a)
F0
F6
a
b
c
d
e
f
Intensity (a.u.)
200
400
600
800
1000
1200
1400
1600
Wave number (cm-1)
(b)
F0
F6
g
h
Q3
Q2
Intensity (a.u.)
850
900
950
1000
1050
1100
1150
1200
Wave number (cm-1)

Figure 15

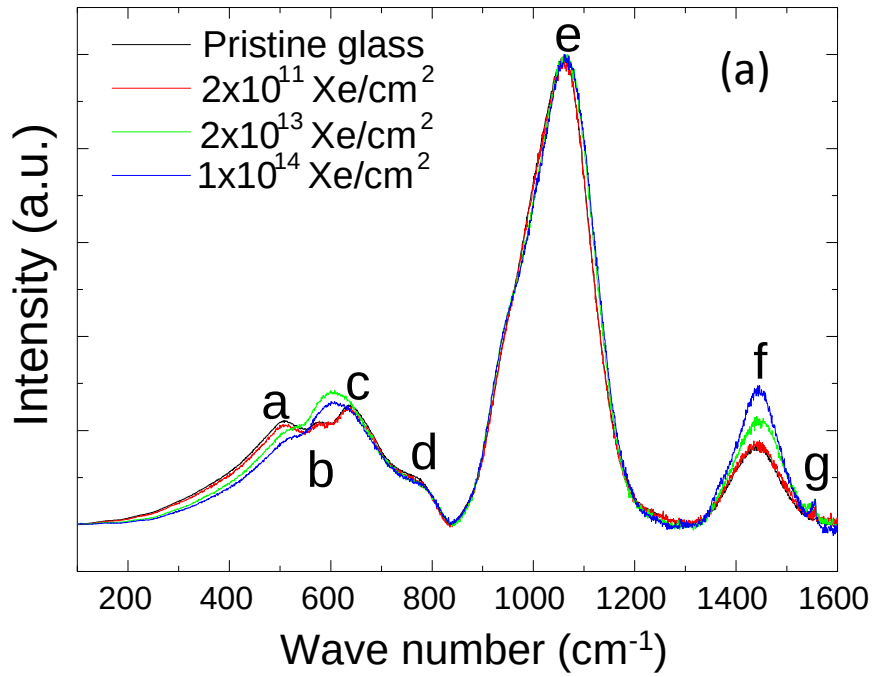
Pristine glass
2x10^11 Xe/cm^2
2x10^13 Xe/cm^2
1x10^14 Xe/cm^2
(a)
a
b
c
d
e
f
g
Intensity (a.u.)
200
400
600
800
1000
1200
1400
1600
Wave number (cm^-1)

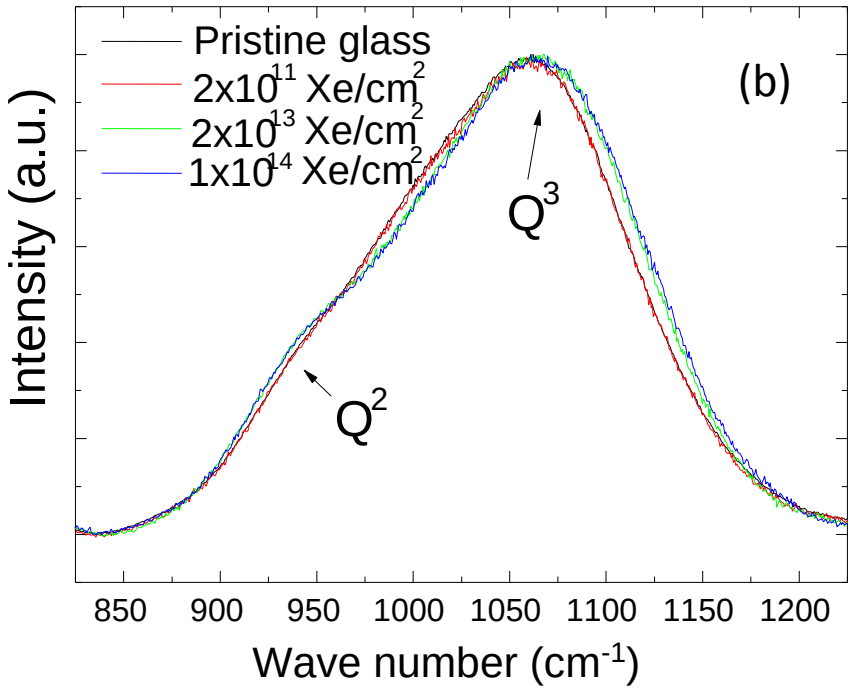
Pristine glass
2x10^11 Xe/cm^2
2x10^13 Xe/cm^2
1x10^14 Xe/cm^2
(b)
Q^3
Q^2
Intensity (a.u.)
850
900
950
1000
1050
1100
1150
1200
Wave number (cm^-1)

Figure 16

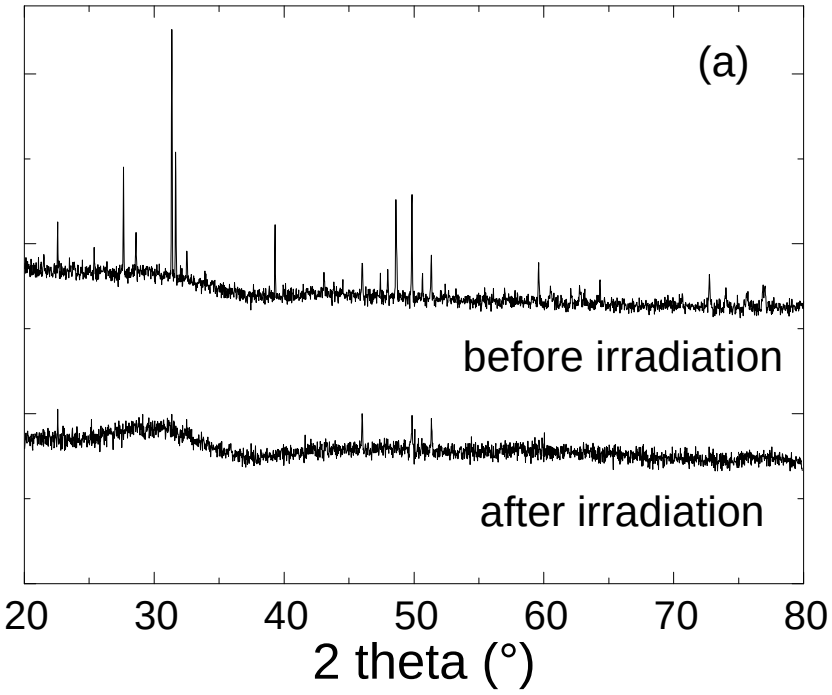
(a)
before irradiation
after irradiation
20
30
40
50
60
70
80
2 theta (°)

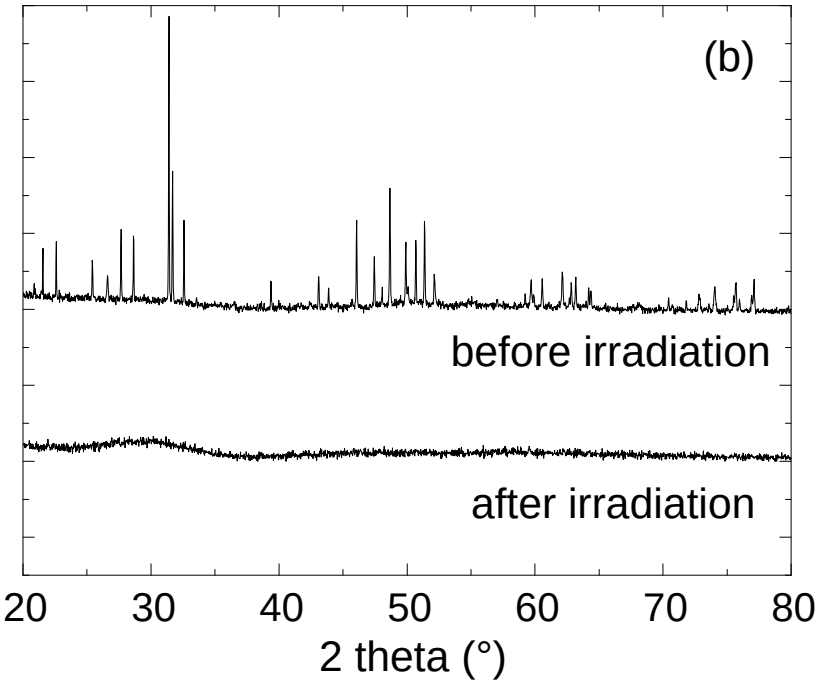
(b)
before irradiation
after irradiation
20
30
40
50
60
70
80
2 theta (°)

Figure 17

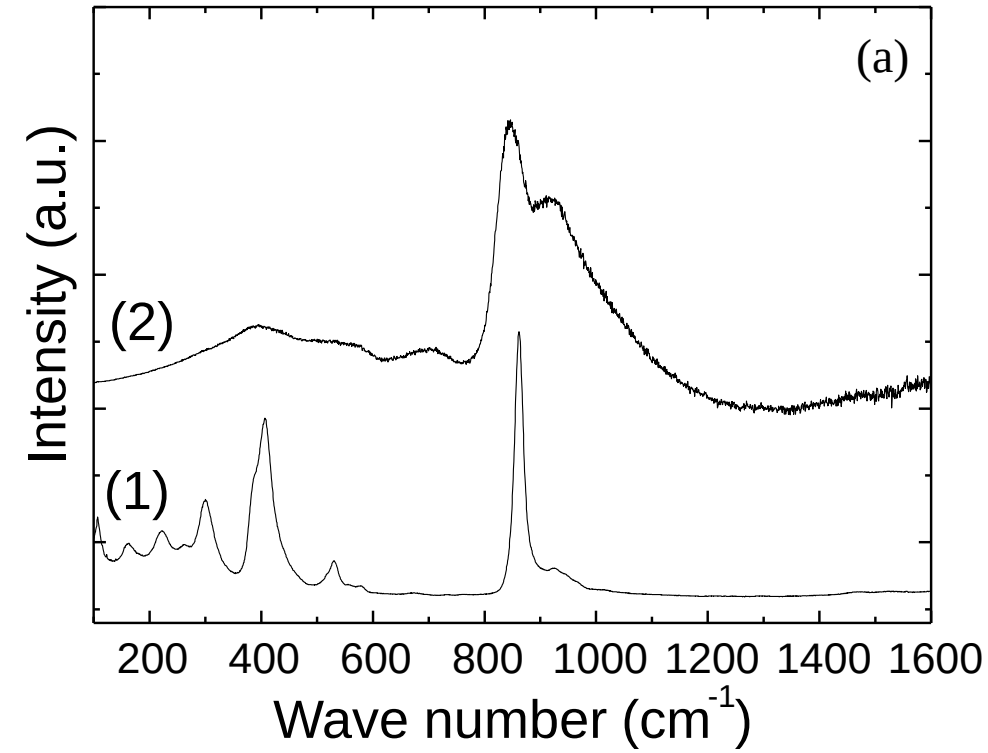
(a)
Intensity (a.u.)
(2)
(1)
200 400 600 800 1000 1200 1400 1600
Wave number (cm-1)

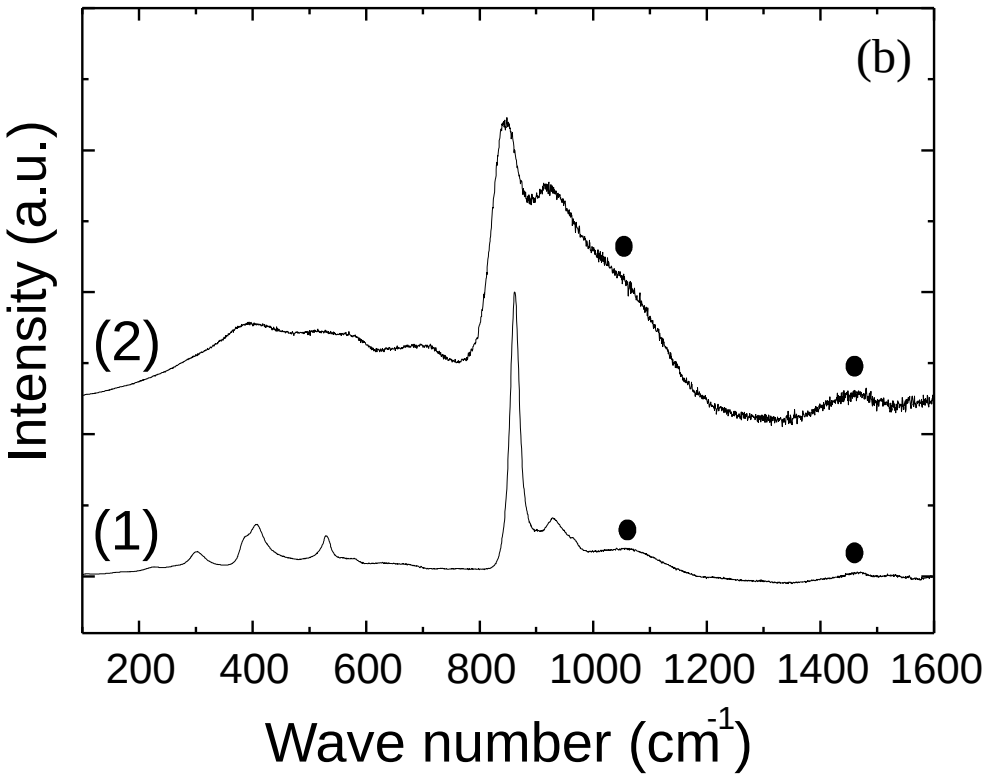
(b)
Intensity (a.u.)
(2)
(1)
200 400 600 800 1000 1200 1400 1600
Wave number (cm-1)

Figure 18

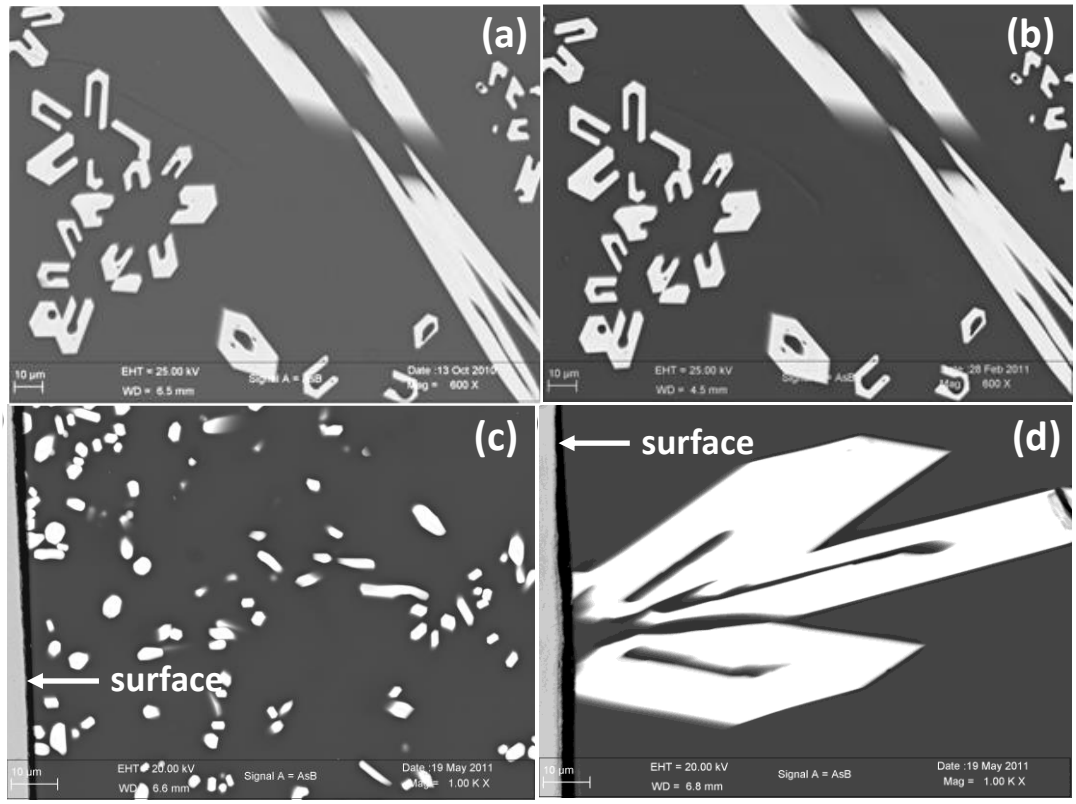

Figure 19

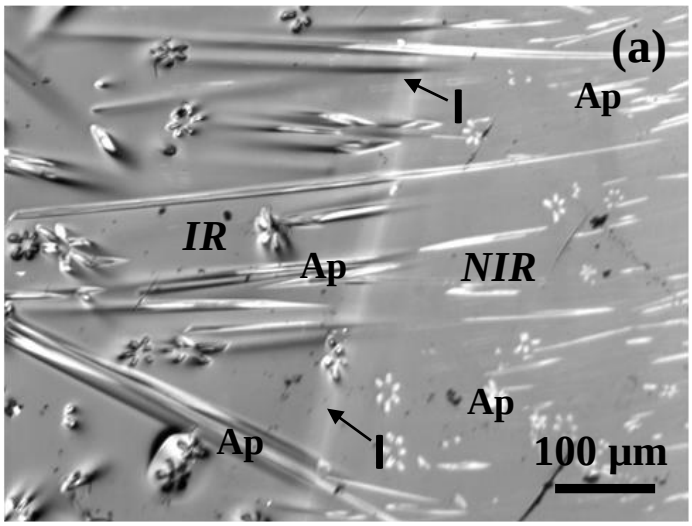
(a)
Ap
I
IR
Ap
NIR
Ap
Ap
I
100 µm

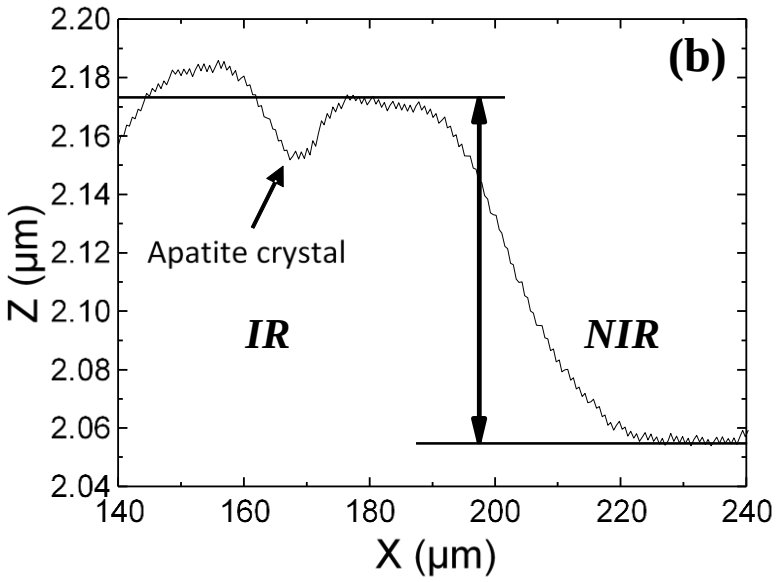
(b)
Z (µm)
X (µm)
Apatite crystal
IR
NIR
2.20
2.18
2.16
2.14
2.12
2.10
2.08
2.06
2.04
140
160
180
200
220
240

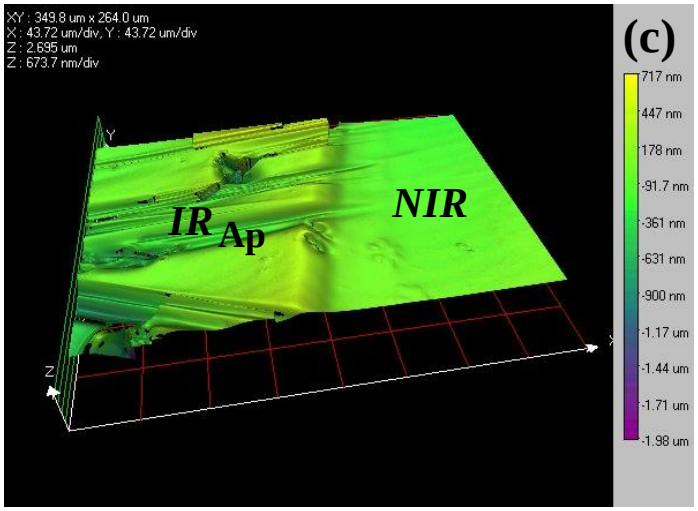
XY : 349.8 um x 264.0 um
X : 43.72 um/div, Y : 43.72 um/div
Z : 2.695 um
Z : 673.7 nm/div
(c)
IR
Ap
NIR
717 nm
447 nm
178 nm
-91.7 nm
-361 nm
-631 nm
-900 nm
-1.17 um
-1.44 um
-1.71 um
-1.98 um